

Near-Infrared Imaging Polarimetry of Young Stellar Objects in rho-Ophiuchi

A. F. Beckford, P. W. Lucas^{*}, A. C. Chrysostomou and T. M. Gledhill
Centre for Astrophysics Research, University of Hertfordshire, College Lane, Hatfield AL10 9AB, United Kingdom

Accepted 2007 . Received 2007 ; in original form Tuesday 17th April 2007

ABSTRACT

The results of a near-infrared (J H K L_P) imaging linear polarimetry survey of 20 young stellar objects in ρ Ophiuchi are presented. The majority of the sources are unresolved, with K band polarizations, $P_K < 6\%$. Several objects are associated with extended reflection nebulae. These objects have centrosymmetric vector patterns with polarization discs over their cores; maximum polarizations of $P_K > 20\%$ are seen over their envelopes. Correlations are observed between the degree of core polarization and the evolutionary status inferred from the spectral energy distribution. K band core polarizations $>6\%$ are only observed in Class I YSOs.

A 3-dimensional Monte Carlo model with oblate grains aligned with a magnetic field is used to investigate the flux distributions and polarization structures of three of the ρ Oph young stellar objects with extended nebulae. A $\rho \propto r^{-1.5}$ power law for the density is applied throughout the envelopes. The large scale centrosymmetric polarisation structures are due to scattering. However, the polarization structure in the bright core of the nebula appears to require dichroic extinction by aligned non-spherical dust grains. The position angle indicates a toroidal magnetic field in the inner part of the envelope. Since the measured polarizations attributed to dichroic extinction are usually $\leq 10\%$, the grains must either be nearly spherical or very weakly aligned. The higher polarizations observed in the outer parts of the reflection nebulae require that the dust grains responsible for scattering have maximum grain sizes $\leq 1.05 \mu\text{m}$.

Key words: polarization – (stars:) circumstellar matter – stars: formation

1 INTRODUCTION

Multicolour imaging linear polarimetry at near-infrared (near-IR) wavelengths is a powerful tool for mapping the dusty discs and envelopes that surround young stellar objects (YSOs). The observed flux distributions and the polarization patterns are both influenced by the distribution and properties of the dust grains responsible for the extinction and the scattering of the light. It can be used to determine which source in a given region dominates the illumination. It can also be used to distinguish between the different mechanisms that produce polarization, since dichroic extinction and scattering processes sometimes produce differing wavelength dependencies.

Generally, the scattering pattern associated with spatially resolved YSOs is centrosymmetric with aligned vectors in the core of the nebula. This pattern of aligned vectors is commonly referred to as the polarization disc. Some YSOs with resolved nebulae differ from the traditionally expected

centrosymmetric pattern by displaying a much broader region of aligned vectors. The most likely cause of this feature is dichroism due to magnetically aligned non-spherical dust grains in the circumstellar disc. Other proposed methods for producing the aligned vector pattern include multiple scattering (Whitney & Hartman 1993) and “illusory disc”, which is an effect caused by limited spatial resolution (Whitney, Kenyon & Gomez 1997; Lucas & Roche 1998).

The ρ Oph star-forming region, at a distance commonly quoted as 160 parsecs, is one of the nearest sites of low-mass star formation. The cloud complex contains a number of distinct dark clouds (Lynds 1962) and filamentary clouds (or streamers), with a total mass estimated to be $10^4 M_\odot$. It has been studied extensively at wavelengths ranging from x-ray to radio (Sekimoto et al. 1997; Girart, Rodriguez & Curiel 2000; Andre, Ward-Thompson & Barsony 1993; Kamazaki et al. 2001). It is known to contain a rich population of young stars associated with circumstellar envelopes and/or discs (Grasdalen, Strom & Strom 1973; Vrba et al. 1975; Elias 1978; Wilking, Young & Lada 1989; Greene & Young 1992; Barsony et al. 1997; Bontemps et al. 2001; Wilking et

^{*} E-mail: P.W.Lucas@herts.ac.uk

Table 1. Rho Oph sample.

Name ^a	Coordinates (2000) ^b		IR Class ^c	Flux (mags) ^d				Alternative ^e Names
	RA	DEC		J	H	K	L	
VSSG1	16 26 21.5	-24 23 07	II	13.49	10.76	8.68	-	EL20, YLW31
GSS30	16 26 21.5	-24 23 07	I	13.89	10.83	8.32	6.1	GY6, WL15
DOAR25	16 26 23.7	-24 43 13	II/D	9.78	9.83	7.73	7.28	GY17, YLW34
WL16	16 27 02.5	-24 37 30	II ?	14.14	10.58	7.92	5.85	GY182, YLW5A
EL29	16 27 09.6	-24 37 21	I	17.21	12.01	7.54	3.88	GY214, YLW7A, WL15
WL20 E	16 27 15.9	-24 38 46	II	13.54	10.78	9.21	8.62	GY240, YLW11B
WL20 W	16 27 15.69	-24 38 43.4	II	-	-	-	-	-
WL3	16 27 19.3	-24 28 45	II	>17.00	14.49	11.20	8.8	GY249, WLY41, YLW41, YLW12D
YLW13A	16 27 19.5	-24 41 40	III	9.42	8.69	8.41	8.22	GY250, WLY40, SR12
YLW13B	16 27 21.7	-24 41 42	II	15.21	11.31	8.41	5.83	GY252, WLY42
WL6	16 27 21.8	-24 29 55	I	>17.00	14.39	10.04	7.13	GY254, YLW14A
WLY43	16 27 27.1	-24 40 51	I	>17.00	13.17	9.46	6.85	GY265, YLW15A
YLW16A	16 27 28.3	-24 39 33	I	>17.00	13.09	9.65	6.68	GY269, WLY44
VSSG18	16 27 28.4	-24 27 21	II	14.47	11.48	9.39	-	GY273, WLY45, EL32, YLW17A
YLW16B	16 27 29.7	-24 39 16	I	>17.00	14.65	11.46	7.63	GY274, WLY46
WLY47	16 27 30.1	-24 27 43	II	15.44	11.64	8.95	-	GY279, EL33, YLW17B
WLY48	16 27 37.2	-24 30 34	I	10.53	8.65	7.42	5.91	GY304, YLW46
WLY51	16 27 40.0	-24 43 13	I	17.12	12.42	8.93	6.15	GY315, YLW45
WLY54	16 27 51.7	-24 31 46	I	16.63	13.50	10.87	4.73	GY378, YLW52
WLY63	16 31 35.5	-24 01 28	I	16.40	12.15	9.29	6.79	L1709B, GWAYL4
WLY67	16 32 01.0	-23 56 44	I	>17.00	13.31	10.43	7.97	L1689-GWAYL6

^a VSSG: Vrba, Strom, Strom & Grasdalen 1975; GSS: Grasdalen, Strom & Strom 1973; DOAR: Dolidze & Arakelyn 1959; WL: Wilking & Lada 1983; EL: Elias 1978; YLW: Young, Lada & Wilking 1986; WLY: Wilking, Lada & Young 1989 Table 2

^b Quoted from SMBAD

^c Wilking, Lada & Young 1989; Andre & Montmerle 1994; Bontemps et al. 2001

^d Wilking, Lada & Young 1989; Greene et al. 1994; Barsony et al. 1997

^e EL: Elias 1978; YLW: Young, Lada & Wilking 1986; GY: Greene & Young 1992; WL: Wilking & Lada 1983; WLY: Wilking, Lada & Young 1989 Table 2; GWAYL: Greene, Wilking, Andre, Young & Lada 1994

al. 2001). Current estimates based on infrared observations put the number of YSOs in the region at approximately 200 (Bontemps et al. 2001). The proximity of ρ Oph to our solar system and the wealth of identified YSOs make it a good site for a polarimetric study of the dusty discs and envelopes surrounding YSOs.

In this paper we present the results of a near-infrared imaging polarimetry survey of young stellar objects in the ρ Oph star-forming region. We compare polarimetric data with assumptions about the evolution of YSOs to determine if there are any correlations between the degree of polarization observed and the evolutionary status determined from the IR SED, also looking for correlations with the object colour. We also present grain scattering models for three of the Class I objects.

In §2 we discuss the observations, in §3 we present the results of the observations, in §4 we discuss the individual sources observed, in §5 we present the computer models, and in §6 we present the conclusions.

2 OBSERVATIONS

The sample contains 18 of the sources identified as Class I, based on the shape of their IR SEDs and spectral indices, from the Wilking, Lada & Young (1989) IR survey of

the ρ Oph region. Subsequent investigation combining sub-millimetre data with the IR data has led to 9 of the sources being re-classified as Class II (Andre & Montmerle 1994). It is these latter classifications that are typically quoted by other authors and are therefore adopted by this paper. The Class II sources were retained in the sample to allow comparisons to be made.

In addition, data has been obtained for a further 2 objects, the Class III object YLW13A and the Class II object WLY47. Table 1 is a complete list of all 20 of the sources, their coordinates, IR classifications, and J, H, K and L magnitudes.

The observations were made at the United Kingdom Infrared Telescope (UKIRT) in Mauna Kea, Hawaii during the nights of 1998 June 17-18, 1999 April 28-May 01, 2000 July 01-03 and 2002 May 15-17. The instrument used was IRCAM with the polarimeter module IRPOL2, designed and built at the University of Hertfordshire. The J (1.2 μm), H (1.6 μm) and K (2.2 μm) broadband filters were used during the 1998, 1999 and 2002 sessions, and the L_P (3.8 μm) band filter was used during the 2000 session. The instrument optics provided a plate scale of 0.286 arcseconds per pixel (0.143 arcseconds with the magnifier). This gave a typical field of view of 36×8 arcseconds when using the magnifier. Prior to the 2000 observing session IRCAM was upgraded, providing a plate scale of 0.0814 arcseconds per pixel and

Table 2. Rho Oph aperture linear polarimetry.

Name	P_{core}^a				P_{max}^b			θ_{disc}^c
	J	H	K	L ^d	J	H	K	
VSSG1	-	1.4±0.8	2.7±1.4	-	-	-	-	-
VSSG1-NW	-	1.3±1.0	3.8±1.4	-	-	-	-	-
GSS30	23.8±0.1	22.7±0.1	15.5±0.1	4.3±1.2	32.9±1.1	41.6±1.3	50.4±1.4	151.2
DOAR25	1.4±0.1	0.8±0.1	1.1±0.1	1.0±0.5	-	-	-	30.1
WL16	-	-	5.1±0.05 ^e	-	-	-	-	33.9
EL29	-	-	8.3±0.06 ^e	-	-	-	35.3±0.6 ^e	28.3
WL20 E	11.5±1.2	-	-	-	-	-	-	38.0
WL20 W	12.5±1.2	-	-	-	-	-	-	33.7
WL3	-	-	2.1±0.2	-	-	-	-	20.3
YLW13A	-	0.98±0.05	0.8±0.05	-	-	-	-	165.3
YLW13A S	-	9.7±0.7	-	-	-	-	-	172.9
YLW13B	-	10.2±0.2	6.3±0.2	4.4±0.1 ^e	-	-	-	11.6
WL6	-	-	3.3±0.5	-	-	-	-	135.5
WLY43	-	3.2±1.4	3.7±1.8	1.8±0.9	-	-	-	-
WLY43-NW	-	4.9±2.1	2.1±1.05	-	-	-	-	-
YLW16A	-	11.4±0.3	10.4±0.2	3.1±1.1	-	21.9±1.3	20.8±1.2	32.6
VSSG18	16.2±7.0	3.1±0.9	2.1±1.1	8.7±1.2	37.2±2.4	22.2±2.2	19.5±2.9	145.0
YLW16B	-	9.7±0.7	6.2±0.4	5.7±0.3	-	-	-	53.8
WLY47	-	5.2±0.02	4.6±0.01	-	-	-	-	179.1
WLY47 "arc"	-	11.3±0.03	7.7±0.02	-	-	28.3±2.1	36.1±2.2	179.1
WLY48	-	-	2.3±0.05 ^e	0.9±0.3	-	-	-	133.5
WLY51	-	9.1±0.2	5.1±0.1	1.6±0.7	-	-	-	23.4
WLY54	9.2±0.05	5.3±0.01	2.4±0.01	4.3±0.01	-	30.6±2.1	43.2±2.3	2.1
WLY63	-	8.0±0.07	3.9±1.8	-	-	-	-	150.1
WLY67	-	9.5±2.2	2.2±1.0	-	-	39.4±3.2	24.1±5.3	0.3

^a Evaluated in 2 arcsecond diameter apertures, except: GSS30, which is evaluated in a 3 arcsecond aperture (to enable comparison with Chrysostomou et al. 1996), and WLY47 arc which is evaluated in a 1 arcsecond aperture. The quoted errors are based on the standard deviation of the polarization within the aperture used to assess the degree of polarization.

^b Evaluated in 0.5 arcsecond diameter apertures, the quoted errors are based on the standard deviation within the aperture.

^c Position angle of the long axis of the disc, evaluated from K waveband data where available

^d Evaluated in 1 arcsecond diameter apertures

^e Shift & Add Result

a field of view of approximately 20×4 arcseconds. During the 2002 observing run UFTI replaced IRCAM3/TUFTI, providing a plate scale of 0.091 arcseconds per pixel and a field of view of 90×15 arcseconds. Typically the seeing was between 0.5 and 1.0 arcsec.

The Wollaston prism mounted in IRPOL2 splits the radiation into the orthogonally polarized beams, usually referred to as the ordinary and extraordinary (o- and e-) beams for historical reasons. A focal plane mask is used to reduce the field of view into two strips, each about 260×50 pixels squared, to prevent the o- and e- beams from overlapping. The half-waveplate in the system is successively rotated through 0, 45, 22.5 and 67.5 degrees. The advantage of this technique is that the intensity of both the o- and e- beams are measured simultaneously, which improves the reliability of the data by greatly reducing the effects of variations in atmospheric transparency and seeing, allowing any variations in atmospheric transparency to be accounted for.

To remove bad pixels on the array a 3-point jitter pattern mosaic, with 5 arcsecond east-west offsets, was used.

2.1 Shift & Add Data

Four of the sample sources, EL 29, WL 16, IRS 54 and IRS 48, were imaged in the K-band using the shift and add image-sharpening technique. This technique involves the taking of very short exposures, which are shifted so that their peak pixels coincide and are then co-added. This is all performed in real-time by the ALICE (Array Limited Control Electronics) electronics system of IRCAM3. The magnifier was adopted during the shift and add runs providing a pixel scale of 0.143 arcseconds.

The main advantage of the shift and add observing technique is in the resolving of compact bipolar nebulae and small polarization discs. However, there are several major limitations of the method. The data are read noise limited due to the short integration times involved, which means that it is much less sensitive than the conventional background limited polarimetry. It is not possible to select or discard frames in a given stack. The method can only be used to observe YSOs that have a prominent compact flux peak.

Table 3. Rho Oph source properties.

Name	α_{IR}^a	Polarization Vector Pattern	Total Intensity Distribution
VSSG1	-0.49	-	Point-like
BKLT ^b	-	-	Point-like
J162618-242818			
GSS30	1.20	Centrosymmetric	Highly extended bipolar nebula
DOAR25	-1.58	Random	Point-like
WL16	0.79	Aligned	Point-like
EL29	0.98	Centrosymmetric	Point-like, polarized intensity images - possibly faint bipolar nebulosity
WL20 E	-0.07	Aligned	Point-like, member of a triple system
WL20 W	-0.07	Aligned	Point-like, member of a triple system
WL3	0.23	Aligned	Point-like
YLW13A	-2.48	Random	Point-like, in the H band there is a possible second source to the south
YLW13A S	-	Random	Point-like
YLW13B	0.08	Aligned	Point-like
WL6	0.59	Aligned	Point-like
WLY43	0.98	-	Point-like (slightly oval)
GY263 ^c	-	-	Point-like
YLW16A	1.57	Centrosymmetric	Extended, bipolar nebula
VSSG18	-0.24	Centrosymmetric	Highly extended cometary nebula
YLW16B	0.94	Aligned	Point-like
WLY47	0.17	Aligned	Point-like, arc of nebulosity to the NW
WLY47 arc	-	Centrosymmetric	Elongated, curved structure
WLY48	0.18	Random	Point-like
WLY51	-0.04	Aligned	Point-like, possible close binary companion
WLY54	1.76	Centrosymmetric	Extended, cometary nebula
WLY63	0.4	Aligned	Point-like
WLY67	0.74	Centrosymmetric	Extended, cometary nebula

^a Wilking, Lada, Young 1989; Bontemps et al. 2001

^b The 2nd source in the VSSG1 field has been identified as possibly being BKLT J162618-242618

^c The 2nd source in the WLY43 field has been identified as possibly being GY263

The source WLY54 was also imaged during the 1998 UKIRT run. Comparisons of the results of both imaging methods reveals that the structure of the total flux distributions and the polarization vector patterns is comparable.

2.2 Data Reduction

The initial reduction of the data was performed using the Starlink software package CCDPACK. Each image was dark subtracted and then divided by a suitable normalized flat-field. Our flatfields for J, H and K are median filtered images constructed from images of the sky taken at each half-waveplate position. For the L band data the flatfields are median filtered images constructed from source images at different offsets. The sky subtraction and the extraction of the o- and e- beam images was performed using the Starlink software package POLPACK.

The images were combined with the same software to generate the Stokes parameters, I, Q and U,

The polarization is

$$P = \frac{\sqrt{Q^2 + U^2 - \sigma^2}}{I} \quad (1)$$

where σ^2 is the variance on Q or U. The position angle of the polarization is

$$\theta = 0.5 \arctan \left(\frac{U}{Q} \right). \quad (2)$$

3 RESULTS

The majority of the sources are point-like, displaying no obvious extended structure. It is possible that these objects may be associated either with compact or faint nebulosity that the detecting instrument is not sensitive to. Five of the sources are clearly associated with extended nebulosity. Two of these appear to have bipolar flux distributions (GSS30 and YLW16A), i.e. they have two lobes of extended nebulosity (evidence for YLW16A having two lobes of extended nebulosity can be seen in flux distribution maps that cover more of the region than can be seen in the polarization data presented here). The remaining objects appear to have cometary morphologies (WLY54, WLY67 and VSSG18), i.e. there appears to be only one lobe of extended nebulosity and any counterlobe that may be present is not visible. In addition to these five objects, the Class II source WLY47 ap-

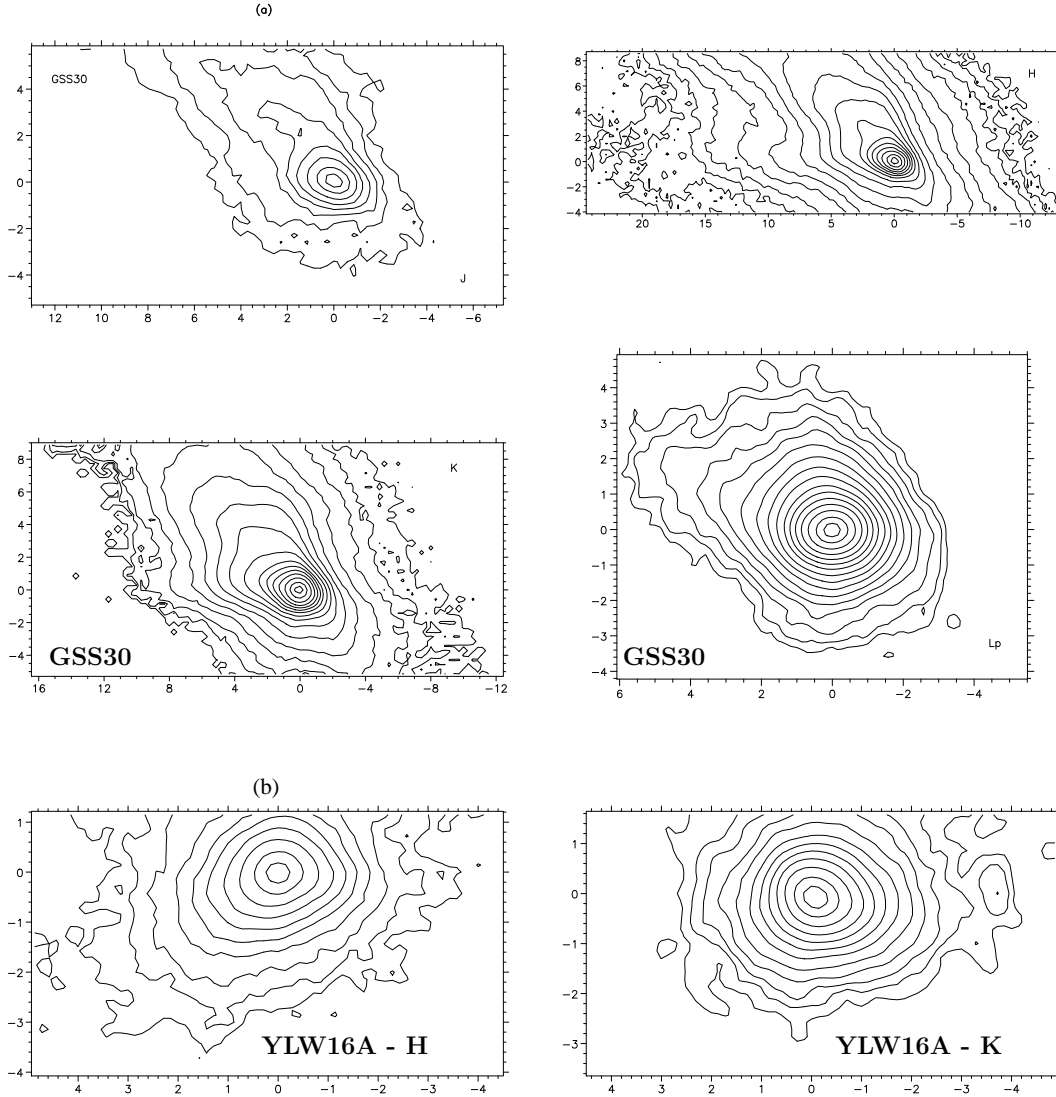


Figure 1. Contour plots of the flux distributions for (a) GSS30, (b) YLW16A. Both GSS30 and YLW16A are bipolar nebulae, although the bipolar nature of YLW16A is only apparent in previously published higher resolution images (see text) and in the polarised flux and degree of polarisation maps (see Figure 4). Contours are normalised and spaced at 0.9,0.71,0.5,0.35,0.25,0.18,0.13,0.088,0.006,0.004,0.003,0.002.

pears to be associated with a nebulous arc a few arcseconds away from the point source.

The flux distributions of the five extended objects and WLY47 are shown in figures 1(a)–(g).

3.1 Polarization

The results of aperture polarimetry on the 20 sources are presented in Table 2. The core polarizations are evaluated in 2 arcsecond apertures, centred on the flux peak. The maximum polarizations are evaluated using 0.5 arcsec apertures, the exact positioning of the centre of these apertures is source dependent but for each source the same position is used at each wavelength. Maximum polarizations are only

shown for sources that are either clearly associated with extended nebulosity, or, in the case of EL29, show a significant spatial variation in fractional polarization within the image, which is attributed to small scale nebulosity that is hidden in the wings of the image profile. Where there is more than one infrared object in the field of view, the degree of polarization of each is shown separately. In total, aperture polarization results are presented for 25 objects.

The polarization vector patterns observed are divided into three categories dependent on their appearance: centrosymmetric, aligned, and random. The pattern is said to be centrosymmetric when the polarization vectors are arranged in a circle (or ellipse) about the main illuminating source. When the polarization vectors appear to be arranged in “parallel lines” the pattern is aligned. In a random pat-

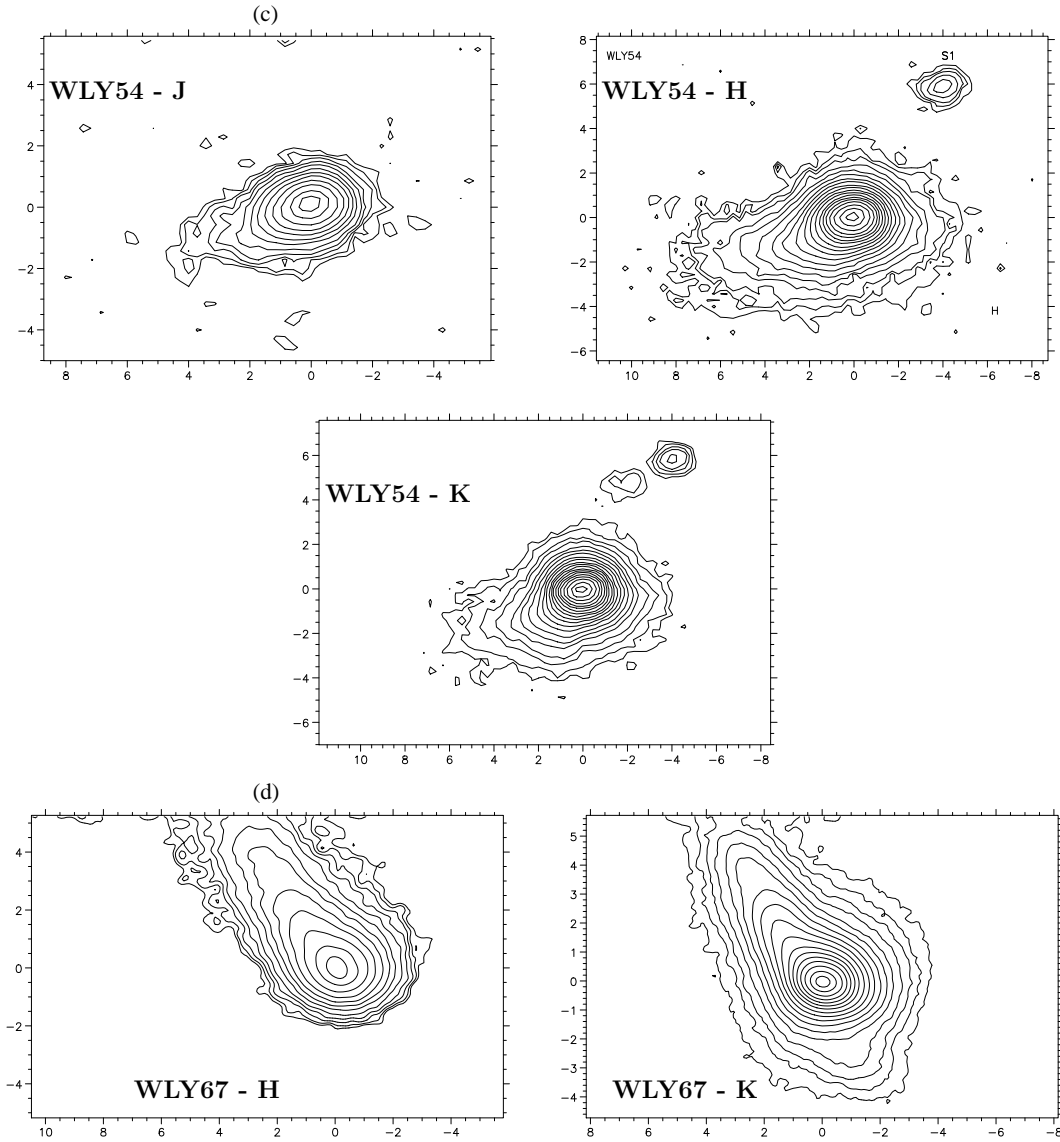


Figure 1. (c) WLY54, (d) WLY67. Both these YSOs display cometary nebulae. Contours are as in Figure 1(a-b)

tern there is no apparent structure to the arrangement of the polarization vectors, indicating that no polarization was detected. In Table 3 the spectral index, α , for each source is presented with a description of both its polarization vector pattern and its structure in the total flux image (i.e. the Stokes I parameter).

4 INDIVIDUAL SOURCES

4.1 Compact Objects

The Class I objects YLW16B, WL6, WLY43, WLY48, WLY51 and WLY63, the Class II objects VSSG1, DOAR25, YLW13B, WL3, WL16 and WL20, and the Class III object YLW13A all have point-like morphologies in both total flux and polarised flux. Several of these objects were found to

be associated with a companion. There is a second object located approximately 1120 AU from the core of WLY43, which has been tentatively identified as GY263, the structure of the companion is point-like. There is a small knot approximately 2 arcseconds (320 AU) to the north of the core of WLY51 at a position angle of approximately 20° , which is surrounded by a horn of material. The appearance of the knot is stronger in the H band, and is only suggested by the K band data. There is a second object to the west of VSSG1. The second object has been identified as possibly being the infrared source BKL T J162618-242818. WL20 has been identified as a triple source by previous authors (Ressler & Barsony 2001). In our polarimetry data two of the members of the system are visible. These are the Class II objects WL20 east (WL20 E) and WL20 west (WL20 W). There is a bridge of material linking both sources.

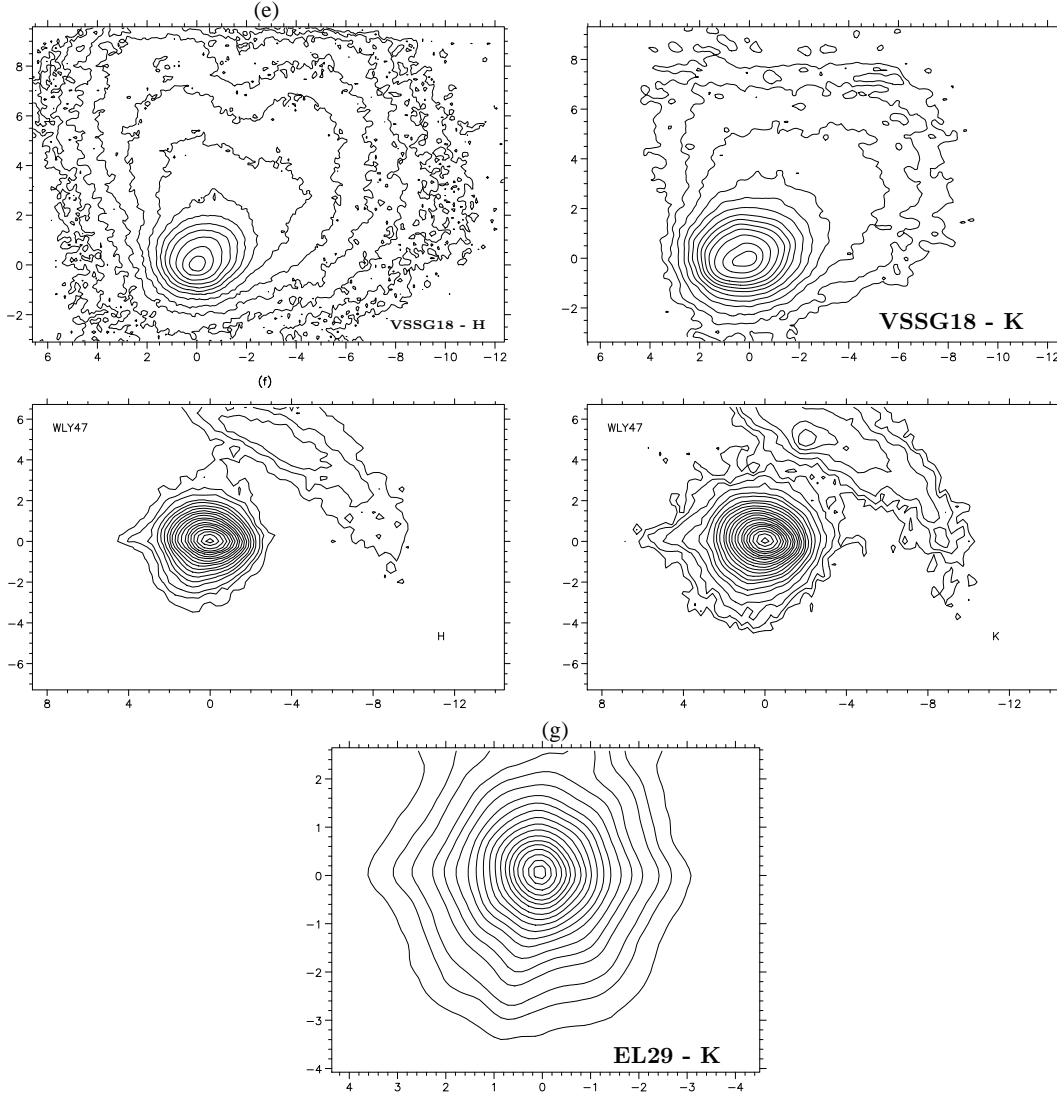


Figure 1. (e) VSSG18, (f) WLY47, and (g) EL29. VSSG18 is a cometary nebula, while WLY47 is a point source which appears to illuminate a detached arc of nebulosity. EL29 is unresolved in this image of the total flux but is resolved in polarised flux (see Figure 8). Contours are as in Figure 1(a-b)

The degree of polarization over the cores of the Class I objects range from $P_H \sim 9\%$ and $P_K \sim 6\%$, for YLW16B, to the very low value of $P_K \sim 2\%$, for WLY48. The levels of core polarization for the Class II objects are at the lower end of those for the Class I objects.

DOAR25 and WL3 only show levels of $P_K \sim 1\text{-}2\%$, whereas the levels observed for YLW13B in the H and K wavebands are $P_H \sim 10\%$ and $P_K \sim 6\%$. The spectral index for DOAR25, $\alpha_{2-14} \sim -1.58$, is the lowest displayed by any of the Class II objects; in some classification schemes it would be considered a Class III object. The spectral index for YLW13B, $\alpha_{2-14} \sim 0.08$, identifies it as a possible transition object, the relatively high levels of polarization would seem to support this. Almost all the compact objects display aligned polarization vectors, the exception being WLY48

which has a random vector pattern. YLW13A is the only Class III source that was imaged. The polarization vectors are best described as being randomly orientated, with an average position angle of $\theta_K \sim 165^\circ$. A $1\text{-}\sigma$ upper limit on the fractional polarization of $<1\%$ is measured in both the H and K wavebands. A second source is visible to the south of YLW13A in the H band. The degree of polarization over YLW13A south is $P_H \sim 9\%$.

4.2 WLY47

WLY47 displays an interesting structure (see Figure 1f). WLY47 appears to be point-like; the interesting feature is the 'arc' of nebulosity that can be seen to the northwest. The

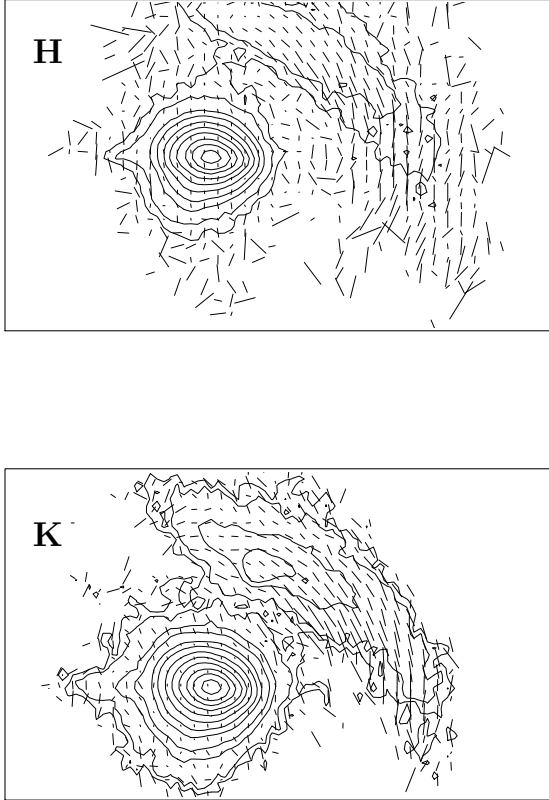


Figure 2. WLY47 polarization. Contour plots of the flux distributions with polarization vectors overlaid for WLY47 in the H (upper) and K (lower) bands. The arc of nebulosity displays a centrosymmetric polarisation pattern, demonstrating that it is illuminated by the adjacent bright YSO. The key is the same length as a 100% vector.

arc extends from the north to the west of the source and is approximately twelve arcseconds (2000 AU) in length. There is evidence of a concentration of flux near the centre of the arc in both the H and K wavebands, possibly indicating that the arc contains a 2nd object. The core of WLY47 is approximately 5.5 arcseconds (880 AU) from the peak of the arc. There is nebulosity surrounding both WLY47 and the arc that is apparent at low signal to noise. HST NICMOS images also reveal the presence of the arc close to WLY47; the arc lies between WLY47 and VSSG18 (Allen et al. 2002).

Figure 2 shows the H and K band polarization vector maps for WLY47. At both the H and K wavebands the polarization vectors across WLY47 are aligned, whilst the vectors over the ‘arc’ follow its structure, in the sense that the polarization vectors over the ‘arc’ appear to be centrosymmetric with respect to WLY47. This indicates that the arc is a reflection nebula illuminated by WLY47. The position angle of the polarization vectors over WLY47 and the peak of the arc are $\theta_K \sim 179^\circ$ and $\theta_K \sim 50^\circ$, respectively. The

levels of polarization observed are higher ($P_H \sim 5\%$ and $P_K \sim 4\%$) than those displayed by the majority of the Class II sources observed. The levels of polarization over the peak of the arc of nebulosity are higher than those seen over the core of WLY47 in both wavebands, ($P_H \sim 11\%$ and $P_K \sim 8\%$). The polarization increases toward the southern end of the arc. This may indicate that the arc does not lie in the plane of the sky and that scattering angle is closer to 90° at the southern end. The maximum levels of polarization given in Table 2 are evaluated over the ‘arc’ and are shown to be $P_H \sim 28\%$ and $P_K \sim 36\%$.

4.3 GSS30

GSS30 has a bipolar morphology, with a northeast-southwest orientation, see Figure 1a and Figure 3. This structure is interpreted as a reflection nebula, with the bright lobes corresponding to reflection from the walls of a bipolar cavity in the circumstellar nebula, which is assumed have been cleared by a bipolar outflow. The northern lobe is brighter and more extensive than its southern counterpart. This has been previously used by Chrysostomou et al. (1996) to estimate the inclination of the system. Their investigation indicated that the system is inclined at an angle of approximately $25^\circ - 30^\circ$ to the plane of the sky, with the northern lobe tilted towards us. Near-IR data covering more of the GSS30 region has revealed an extensive bipolar nebula that contains three distinct sources (Chrysostomou et al. 1996). The main illuminating source is given the designation IRS1; the other two sources are IRS2 and IRS3, both lie in the northern lobe of nebulosity.

The polarization vector map is shown in figure 3(a). The polarization vector pattern is centrosymmetric in the outer regions, becoming more elliptical towards the main illuminating source (IRS1). There is evidence of a narrow polarization disc over the core of IRS1 with a position angle $\theta_K \sim 151^\circ$, at the J, H, K and L_P wavebands. The polarization disc runs perpendicular to the orientation of the bipolar extension. There is no apparent offset between the position of the disc and the central flux peak. To the south of IRS1, along the polarization disc, the vectors experience a 90° flip in their orientation, returning to the centrosymmetric pattern. This return to the centrosymmetric vector orientation is not observed at the northern end of the disc in the J, H and K waveband maps, a feature previously noted by Chrysostomou et al. (1996). In the L_P band map a return to centrosymmetric pattern is seen at both ends of the polarization disc. These reversals are predicted in Monte Carlo multiple scattering models that do not include dichroic extinction effects (e.g. Figure 12 of Lucas & Roche 1998). The return to a centrosymmetric pattern at the ends of the polarization disc is caused by the transition from the optically thick part of the disc to the optically thin region where single scattering dominates the pattern, as opposed to multiple scattering. It is likely that the absence of this reversal at the northern end of the disc in the shorter wavelength data is due the greater extinction at shorter wavelengths. Greater extinction would increase the size of the optically thick, multiple scattering region and it would also strengthen any dichroic extinction effects which may also be contributing to the observed polarisation disc, if the magnetic field has a toroidal structure along this line of sight.

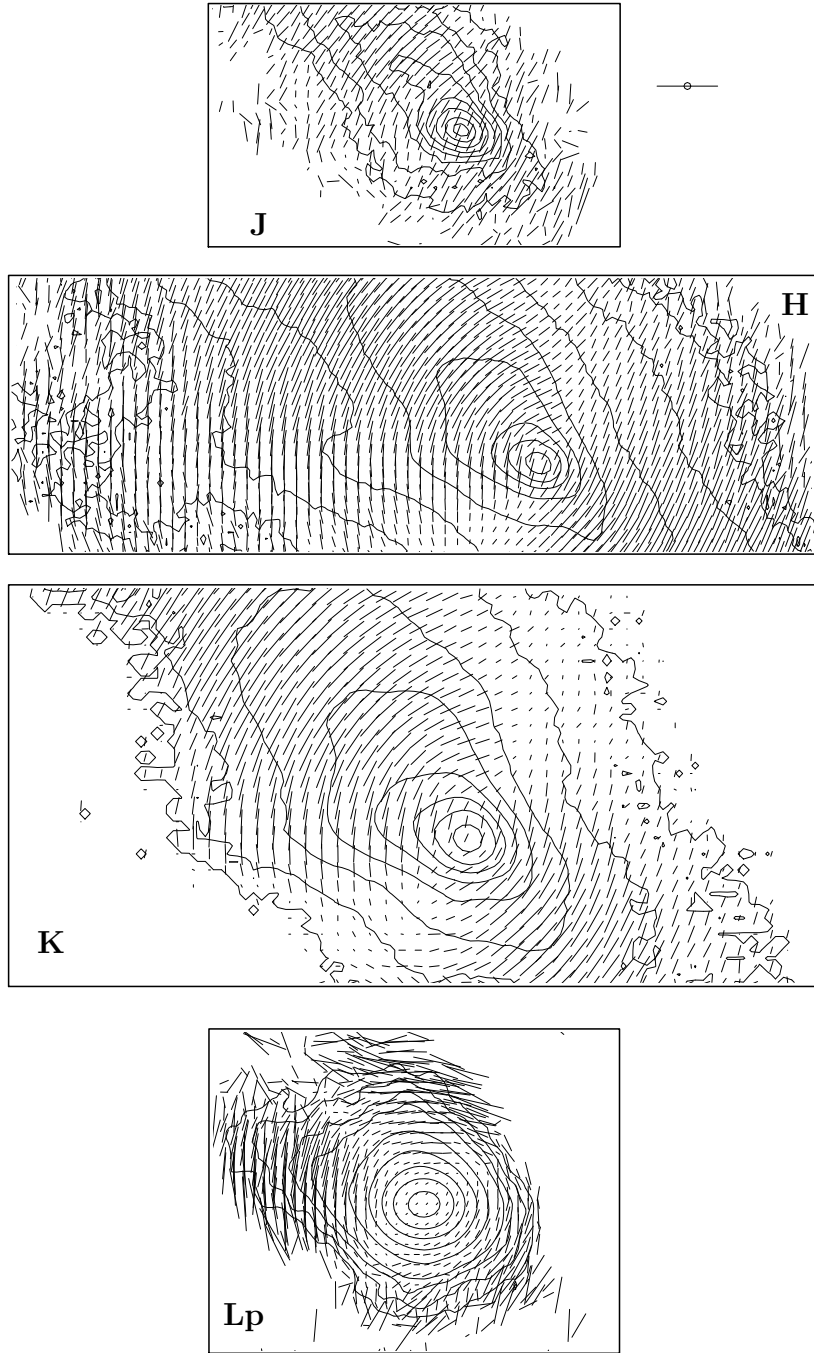


Figure 3. GSS30 polarization. (a) Contour plots of the flux distributions with polarization vectors overlaid in the J (top), H (upper middle), K (lower middle), and L_P (bottom) bands (the key is the same length as a 110% vector).

In figures 3(b) and (c) images of the degrees of polarization and polarized flux at the H, K and L_P bands are shown, respectively. (Polarized flux in each pixel is the product of flux and degree of polarisation). The H, K and L_P band degree of polarization maps have a lower polarization region representing the polarization disc. The low polarization region is surrounded by a higher polarization region, which marks the extent of the nebulosity shown in figure 3(a). In the L_P band map there is also a lower polarization region that extends in the direction of the polarization disc axis, for

the length of the bright north lobe. This region is narrower than the low polarization region that marks the polarization disc. A similar feature is not seen in either the H or K band maps. The L band observations penetrate low density matter and any knots of dust in the bipolar cavity to show the influence of the dense material more clearly. It is likely that the low polarization region seen at L_P band along the polarization disc axis is simply due to the smaller scattering angle for material in the walls of the bipolar cavity that is projected along the axis, compared to off-axis loca-

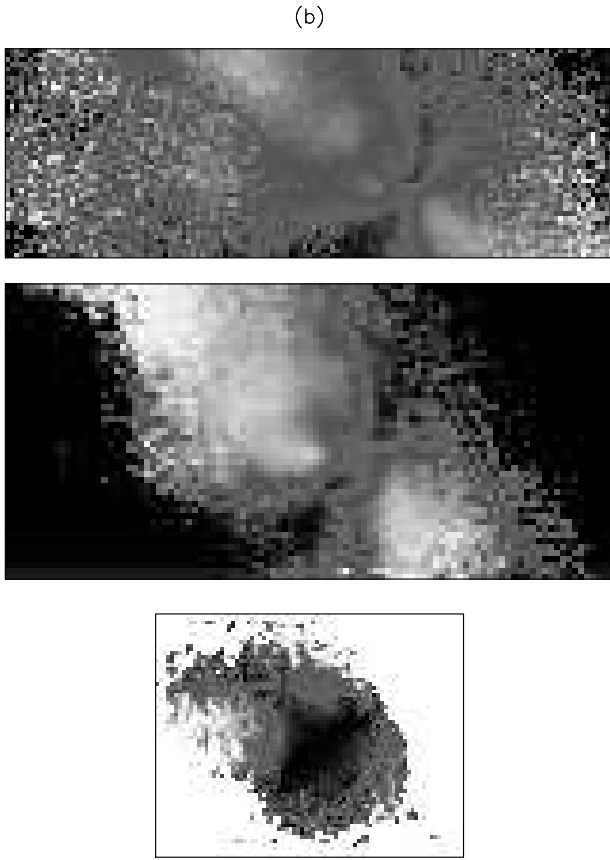


Figure 3. (b). Degree of polarization maps for GSS30. The panels are for the H (top), K (middle), and L_P (bottom) bands.

tions. At shorter wavelengths this effect (previously seen in IRAS 04302+2247 by Lucas & Roche 1997) may be obscured by low density matter within the cavity. Future studies of GSS30 should look at the object at radio and millimetre wavelengths to determine the appearance of the disc, see Zhang, Wootten & Ho (1997).

In the L_P band polarized flux map, there appear to be three lobes. The smallest is the southern lobe seen in the flux distribution. The larger northern lobe that is apparent in the total flux distribution is seen as two lobes in the polarized flux map. We interpret this as a simple consequence of the region of low polarization located between the two lobes. In the H and K band maps (figure 3(c)) the structure revealed is similar to that seen in the flux distribution but the flux distribution appears pinched in the disk plane, revealing the bipolar nature of GSS30 more clearly. This is due to the low polarization in the disk plane, caused by multiple scattering in this optically thick region. There are two lobes that extend northeast and southwest. Close to IRS1, where the polarized light is brightest, the lobes appear to extend more along an east-west axis. This inner east-west extension is not seen in

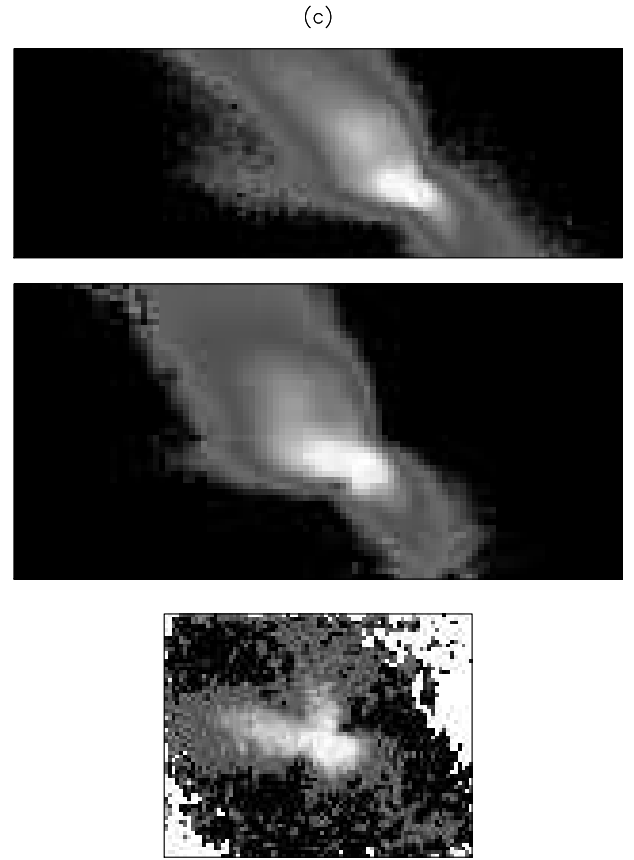


Figure 3. (c). Maps of the polarized flux for GSS30 in the H (top), K (middle), and L_P (bottom) bands.

the total flux distribution, but it does roughly align with the horn of nebulosity that extends to the east of the northern lobe. The eastern extension in polarized flux is due to a region of high polarization shown in figure 3(b). This may be caused by a region of low extinction inside the cavity to the east of IRS1, which would minimise the amount of depolarization due to multiple scattering.

4.4 YLW16A

The data presented covers the central 7×5 arcseconds (1125×800 AU) of the YLW16 region. The structure revealed by the polarization data in Figure 4 is a bipolar nebula, with an approximately east-west extension; in the H band the inner contours have a more northwest-southeast orientation. The bipolar structure is less obvious from the Stokes I contours (see Figure 1b) but it is clear in the higher resolution HST NICMOS image shown in figure 15 (see also Allen et al.2002). Previous authors have shown that the nebula surrounding YLW16A has a radius of approximately 3400 AU (Aspin, Casali & Walther 1989; Lucas & Roche

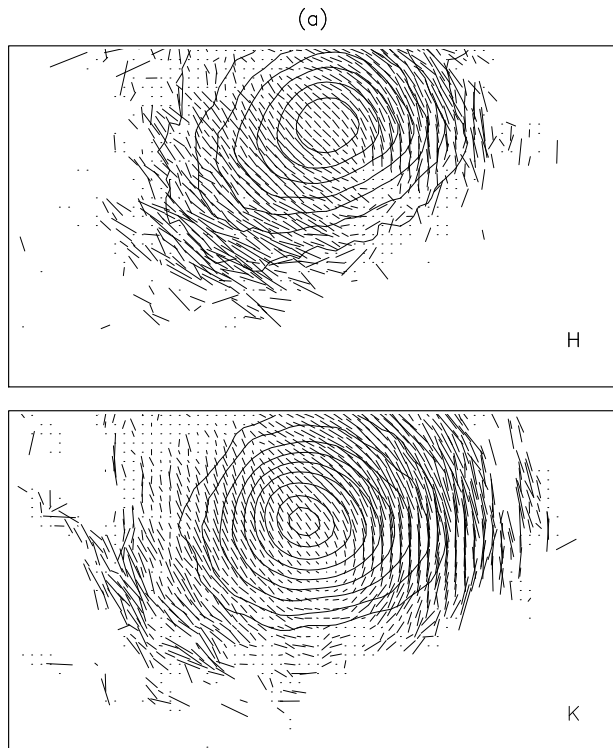


Figure 4. YLW 16A polarization. (a) H and K band contour plots of the flux distributions with polarization vectors overlaid, the key is the same length as a 50% vector, (b) Degree of Polarization maps, and (c) Polarized flux distribution maps for YLW16A. The data are (b) scaled between 2% (black) and 45% (white), and (c) on a logarithmic scale between 1.6 (black) to 2.5 (white) at H and 1.6 (black) to 3.1 (white) at K.

1998). Lucas & Roche (1998) commented that the outer contours at H-band have an interesting structure reminiscent of an arrowhead. At K-band they found that this structure was less prominent. The HST NICMOS images of the source reveal two non-point sources at the position of YLW16A. The resolved nature of these sources make it difficult to determine whether there are actually two sources, or one source being seen in scattered light. Their appearance at 1.1 and 1.6 μm suggests that there is only one source.

The polarization vector pattern is centrosymmetric in the outer regions. In the core region there is a broad polarization disc which is far more extended along the axis of the bipolar nebula than is typical and is evident in both the H and K band maps (see figure 4(a)). The strength of this feature strongly implies that it is produced by dichroic extinction by grains whose short axis is preferentially aligned with the disc plane., since multiple scattering models with spherical grains do not reproduce it, see section 5.3. Furthermore, the position angle of polarisation of the adjacent unresolved source YLW16B is very similar to that of the po-

larization disc in YLW16A, which also suggests that dichroic extinction is operating.

In order to test this hypothesis we removed the dichroic component by subtracting the average Q/I and U/I values for YLW16B from the Q/I and U/I frames for YLW16A. The resulting effect on the polarization vector pattern of YLW16A is that the H band polarization disc is not as broad as shown in figure 3(a), and it has a position angle of $\theta_H \sim 0^\circ$. In the K band the polarization disc is no longer clearly visible. This is what would be expected if dichroic extinction is primarily responsible for the polarization disk, so the evidence supports this interpretation.

There is no apparent offset between the polarization disc and the central flux peak. The polarization disc is also observed to be approximately perpendicular to the direction of the inner contours, with a position angle of $\theta_K \sim 32^\circ$ and $\theta_H \sim 40^\circ$. This is the largest variation in the position angle of the polarization disc between wavebands shown by any of the sources. In the K band polarization vector map, following the length of the polarization disc to the south the vectors return to the centrosymmetric pattern. The same is not seen to the northern end of the polarization disc in either the H or K bands. The similarity in the degree and position angle of the dichroic aspect of the polarization for YLW16A and YLW16B suggests that it is possible that there is a strong feature at this point that is responsible.

Figures 4(b) and 4(c) are images of the degree of polarization and the polarized flux in the H and K bands. In the degree of polarization maps there is a region of low polarization that marks the position of the polarization disc, the lowest levels of polarization are observed at the ends of the polarization disc. Higher polarization regions are observed to either side of the polarization disc.

In the H band polarized flux map there are two lobes that extend roughly northwest and southeast. The southern lobe is the largest. The polarized light is brightest in a central region that is roughly centred on the core. The polarized light is pinched to the south of the core of YLW16A; a similar pinching is not seen to the north. In the K band the structure revealed gives the polarized light the appearance of being an inverted V. The brightest region of polarized light is offset from the core, lying almost central to the eastern lobe. A second less brilliant region is seen in the western lobe.

YLW16A has the lowest levels of maximum polarization of all the extended sources, but it does not have the lowest core polarization. In Table 2 the core polarization of YLW16A in the K band was shown to be $P_{core} \sim 10\%$, with a maximum polarization of $P_{max} \sim 21\%$. The polarization data does not cover the full extent of the YLW16A, so this may well be an underestimate for P_{max} .

4.5 WLY54

The structure revealed in Figure 1c indicates that WLY54 is a cometary nebula. The tail of nebulosity extends roughly to the east of the core; the H band data indicates that the tail extends for at least 1500 AU. In the H and K band total flux distribution maps there is a second 'object' (labelled S1) approximately 720 AU to the northwest of the core, the nature of this object is not known. There does not appear to be any nebulosity extending from WLY54 to surround S1.

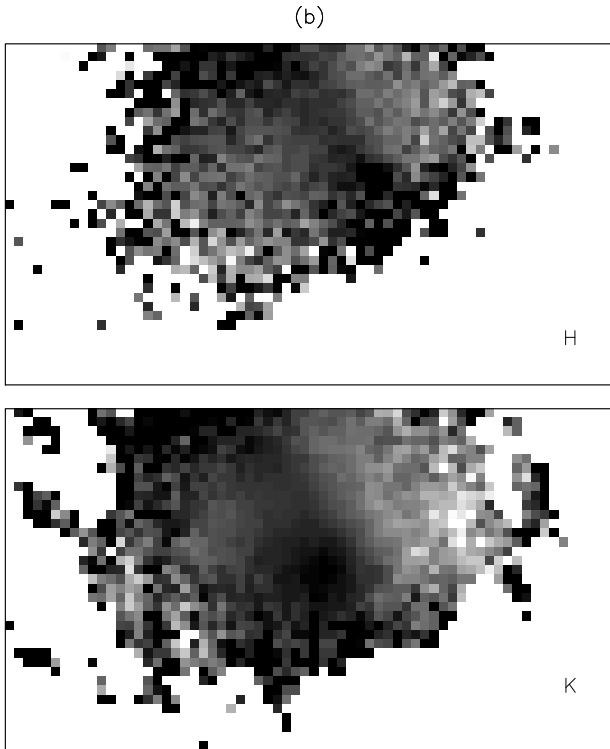


Figure 4. (b). Degree of polarization maps for YLW16A.

However, in the K band there is a second knot of nebulosity between WLY54 and S1.

The polarization vector maps in the J, H and K band are presented in figure 5(a). The vector pattern is centrosymmetric. There is evidence in the J and H band maps of a narrow polarization disc with a position angle $\theta \sim 0^\circ$, which lies over the central flux peak. The polarization discs observed for other objects appear to be perpendicular to the orientation of the extended nebulosity; this is not the case for WLY54. In WLY54 the angle between the polarization disc and the direction of the extension is approximately 109° .

The polarization vector pattern indicates that WLY54 might be a bipolar system that is at an inclination angle that minimizes the amount of counterlobe visible. The position angle of the polarization disc relative to the direction of the extension would make sense if there were a source of foreground extinction that is obscuring the northern regions of WLY54.

The core polarization levels seen are approximately 2%, 5%, and 9% at the K, H, and J wavebands respectively. This is at the lower end of the levels observed for Class I objects, and is much lower than the levels for the other extended sources. The maximum polarizations for WLY54 are assessed over the cometary tail at a distance of approximately 6 arcseconds (1000 AU) from the flux peak. The

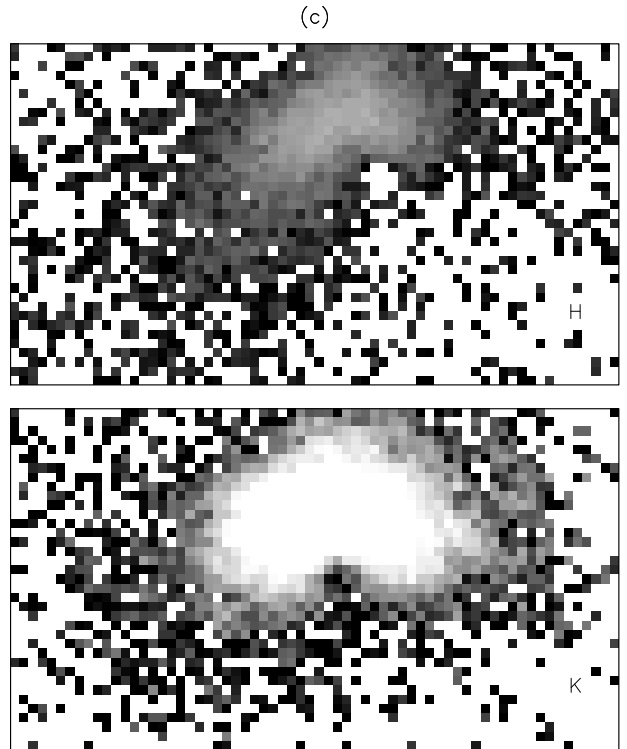


Figure 4. (c). Maps of the polarized flux for YLW16A.

maximum polarizations at H and K are approximately 30% and 43% respectively.

The degree of polarization maps in the H and K bands (see figures 5(b) and (c)) reveal a low polarization region over the core of WLY54. A higher polarization region is seen over the cometary extension, and a smaller higher polarization region is seen to the west of the core. The knot S1 is visible in the H band degree of polarization map; in the K band map S1 and S2 appear as a single “stream”. In figures 5(b) and (c) the polarized flux maps at the H and K bands are presented. The structure of the polarized light is similar to the total flux distribution. The structure of the knots is not seen clearly in either the H or K band polarized light map. In the H band there is a slight bipolar pinching to the south of the core; the pinching is not seen in the K band.

4.6 WLY67

WLY67 has a cometary morphology, see Figure 1d and Figure 6. The cometary tail extends to the north of the core for at least 7 arcseconds (1120 AU). In the K band the structure of the tail appears to narrow with distance from the core, a similar narrowing is seen in the H band data. To the south of the core in the K band there is a small broad horn of nebulosity that is not visible in the H band.

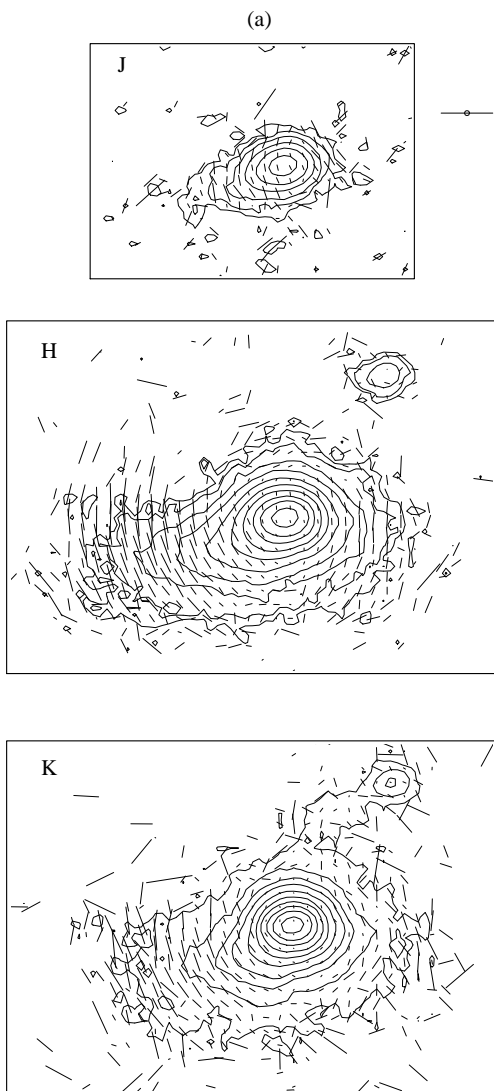


Figure 5. WLY54 polarization. (a) J, H and K band contour plots of the flux distributions with polarization vectors overlaid, the key is the same length as a 100% vector, (b) Degree of Polarization maps, and (c) Polarized flux distribution maps, for WLY54.

The polarization vector map presented in figure 6 reveals that the vectors over the cometary extension have a centrosymmetric orientation. The vectors to the south of the core also appear to be centrosymmetric. In the H band there is evidence of a narrow polarization disc with a position angle of $\theta \sim 90^\circ$ over the core. The polarization disc is not seen in the K band.

In polarized light the structure revealed for WLY67 is similar to that observed for the total flux distribution. There is no significant pinching towards the ends of the polarization disc defined by the vector map.

4.7 VSSG18

VSSG18 is the only Class II source in the sample that is associated with a highly extended nebula (see Figure 1e, Figure 7). All other non-Class I sources appear to be point-like in nature; suggesting that any associated extended nebulosity has already dispersed leaving only a more compact structure. This is consistent with star formation models, which predict that by the Class II stage of evolution an object will have lost its extended envelope. The extensive nebulosity of VSSG18 suggests that its evolutionary status is actually similar to that usually associated with Class I sources. If this is so, the weak mid-IR and far-IR emission could be explained if the disc axis is oriented close to pole-on (see Whitney et al. 2003) but we would then expect the central protostar to appear much brighter relative to the surrounding nebula. A possible alternative explanation is a gap in the inner accretion disc, perhaps due to binarity, which would reduce the amount of warm dust emitting at the IRAS wavelengths.

The nebulosity associated with VSSG18 has a cometary morphology, which extends roughly to the northwest. The nebulosity broadens with distance from the core, giving the material a fan-like appearance. The H and K band flux distribution maps show that the cometary nebulosity extends for at least 2500 AU. In the J band the structure of the nebulosity differs from that observed in the H and K bands. The nebulosity appears to extend to the north; approximately 3200 AU from the core the nebulosity is “pinched”, before broadening. HST NICMOS data reveals a large sigma-shaped nebula; the nebulosity extends for at least 3800 AU, the exact location of the main illuminating source is not identified (Allen et al. 2002).

The polarization vector maps in the H and K bands are presented in figure 7. The vectors over the extended nebulosity are centrosymmetric. Atypically, the vectors over the core are aligned with a position angle of $\theta \sim 145^\circ$, placing them parallel to the direction of the extension. The other objects that have a centrosymmetric polarization vector structure show aligned vectors that are approximately perpendicular to the direction of the extended nebulosity. To the southern end of the aligned vectors there is no clear evidence of a return to the centrosymmetric pattern. The amount of information in the J band polarization vector map (not shown) is limited, but it can be seen that vectors over the core are at a position angle of 0° and the vectors over the extended nebulosity are centrosymmetric.

The structure of the polarized light reveals a bright region approximately centred over the core surrounded by a faint region that marks the extended nebulosity. There is no evidence of the typical bipolar pinching at the ends of the polarization disc.

4.8 EL29

EL29 (see Figure 1g, Figure 8) is one of the four objects that were imaged using the shift and add image sharpening technique during the UKIRT 1999 observing run. Although EL29 has been studied before at near-IR wavebands this is the first time it has been looked at using high resolution linear polarimetry. The structure of the total flux distribution revealed indicates that EL29 is a point-like object. Previous

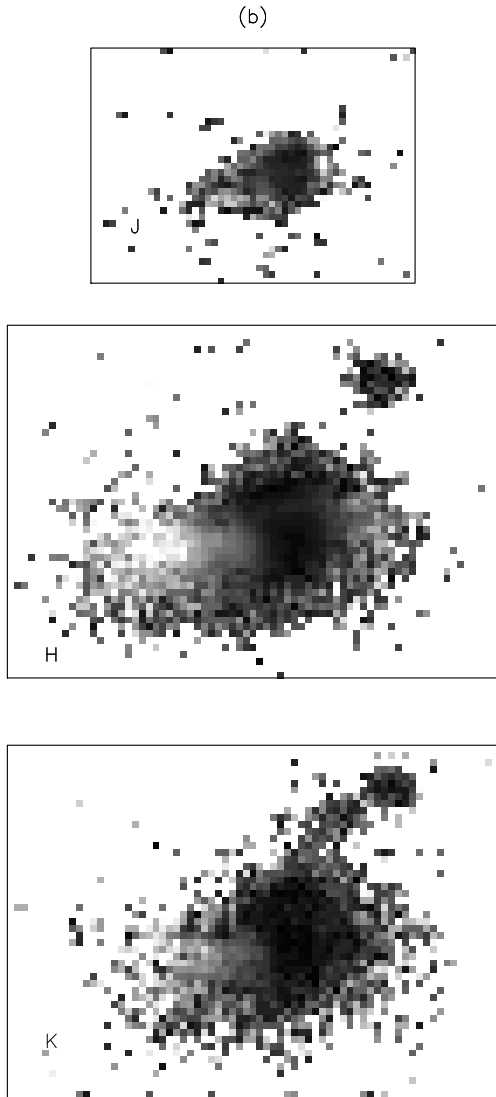


Figure 5. (b). Degree of polarization maps for WLY54.

studies have indicated that EL29 may be associated with extended nebulosity (Elias 1978; Duchene et al. 2004).

EL29 differs from the other point-like objects discussed previously (see §4.1); instead of the aligned or random polarization vector pattern, the vectors are centrosymmetric and they extend for approximately 7 arcseconds (1120 AU) from the core. There is a narrow polarization disc over the core, with a position angle $\theta_K \sim 20^\circ$. To the northern end of the disc the level of polarization decreases to approximately $P \sim 0\%$, a similar decrease is seen to the southern end of the disc. The polarization vectors return to the centrosymmetric pattern after the ‘nulls’.

The pattern seen for the polarization vectors strongly suggests that a faint bipolar nebula surrounds EL29. Figures 8(b) and (c) are maps of the degree of polarization and the polarized intensity. In figure 8(c) there is a disc-like region of lower polarization surrounded by a higher polarization re-

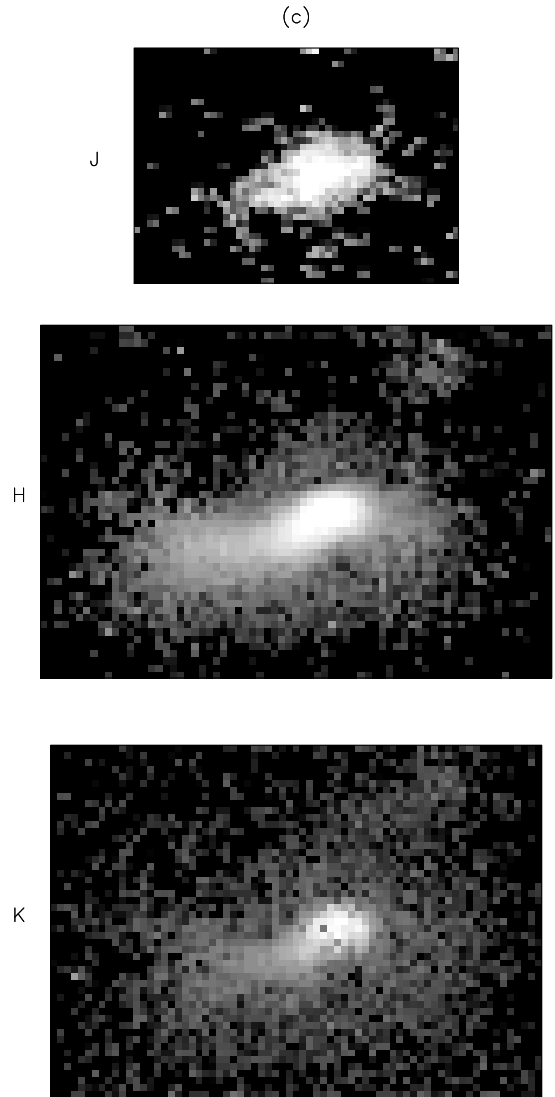


Figure 5. (c). Maps of the polarized flux for WLY54.

gion. At the ends of the disc, two polarization nulls are seen. The structure revealed in the polarized intensity map is not the point-like object seen in the total flux distribution. Instead in polarized light EL29 appears to be elongated, with a southeast-northwest orientation. There is a slight ‘pinching’ of the polarized light that is characteristic of a bipolar object.

This result for the polarised flux image has recently been independently confirmed by the conference report of Huélamo et al.(2007), which contains higher resolution data from the VLT. Deep infrared imaging by Ybarra et al.(2006) also reveals the extended nebulosity and shows that there are H₂ emission features within the outflow cavities, which are oriented southeast-northwest as our polarised flux image implied.

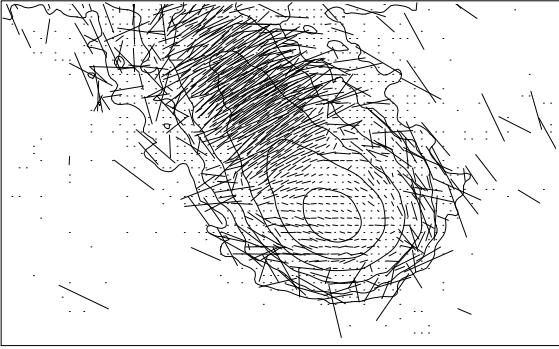


Figure 6. WLY67 polarization (K band). A contour plot of the flux distribution with polarization vectors is overlaid. The key length is the same as a 50% vector.

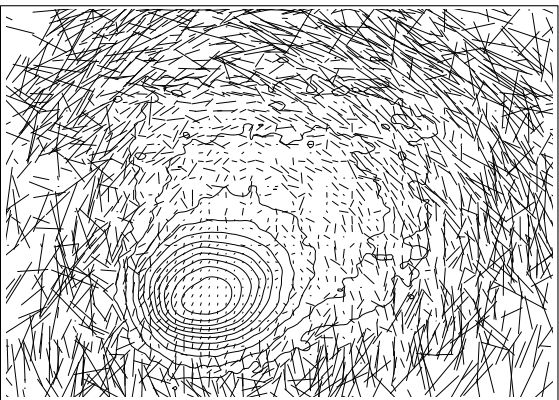
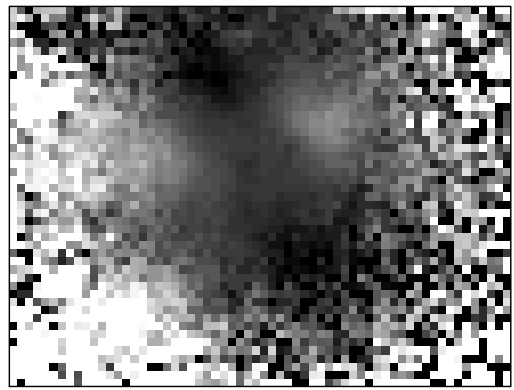
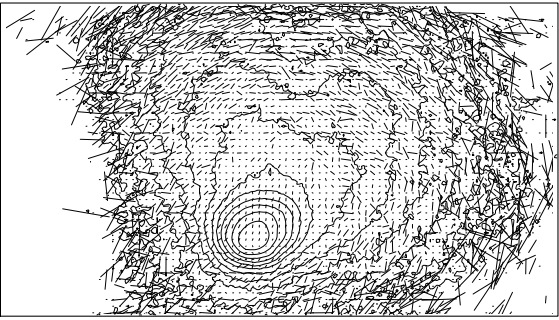
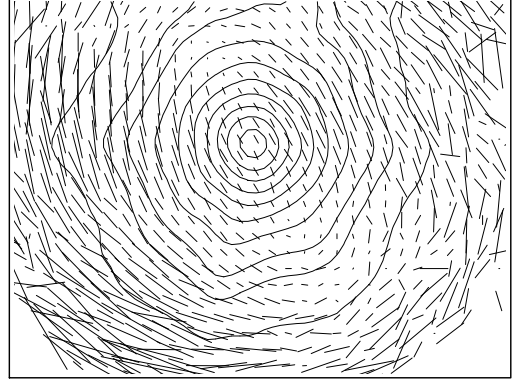


Figure 7. VSSG18 polarization. Contour plots of the flux distributions with polarization vectors overlaid for VSSG18. The key is the same length as a 50% vector.

Figure 8. EL29 polarization. (a) Contour plot of the flux distribution with polarization vectors overlaid, the key is the same length as a 50% vector, (b) Degree of Polarization map, scaled between 0% (black) to 40% (white) and (c) Polarized flux distribution map for EL29, plotted on a logarithmic scale between 0 (black) to 2.4 (white).

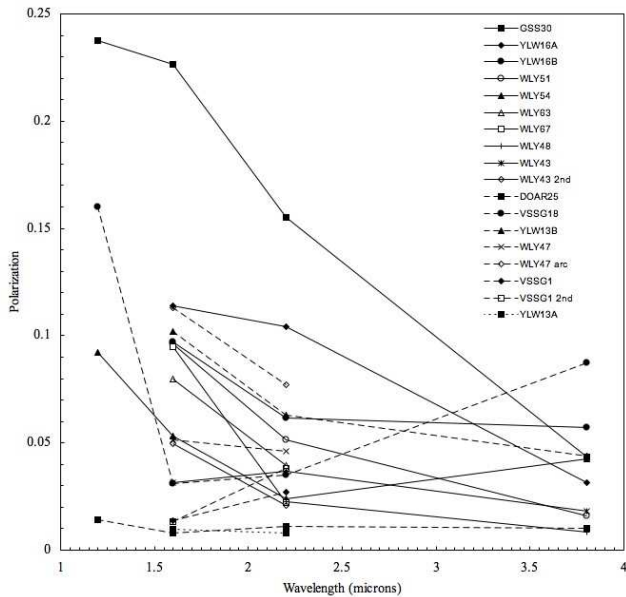


Figure 9. Wavelength dependence of the core polarizations. Solid lines are class I YSOs, dashed lines are class II and dotted lines class III. The behaviour of the polarization with wavelength indicates that for the majority of the sources dichroism is important in the core regions.

4.9 Discussion

4.9.1 Wavelength Dependence

The wavelength dependence can reveal information about the nature of the mechanisms responsible for the scattering and absorption of light in an YSO. The wavelength dependence in the core regions for the 18 objects that were observed at multiple wavebands is shown in figure 9. The key indicates the identities of individual sources. The wavelength dependence seems to be independent of the IR classification; similar behaviour is observed for Class I, II and III YSOs. Most of the objects show a change of a few percent, typically 3 – 4%, between 1.6 μm and 2.2 μm .

In the majority of the objects the degree of polarization decreases with increasing wavelength. This is the expected wavelength dependence if dichroism is the main mechanism responsible for the polarization of light. However it is also possible for scattering to produce the same wavelength dependence if: (i) the polarization within the adopted aperture integrates over a complicated polarization structure (Whitney et al.1997); or (ii) the measurement is of a polarization disc of a bipolar source where most photons have been multiply scattered (Lucas & Roche 1998). We think it very likely that the observed wavelength dependence in the point sources is due to dichroic extinction in most cases. The alternative explanation, that the measured polarisation is due to scattering in spatially unresolved reflection nebulae with complicated polarization structures, is not likely to be such a common occurrence.

Four of the YSOs investigated show an increase in the level of polarization with increasing wavelength: VSSG1, BKLT J162618-242818, WLY43, and the WLY47 ‘arc’. This indicates that scattering is important in these sources, since

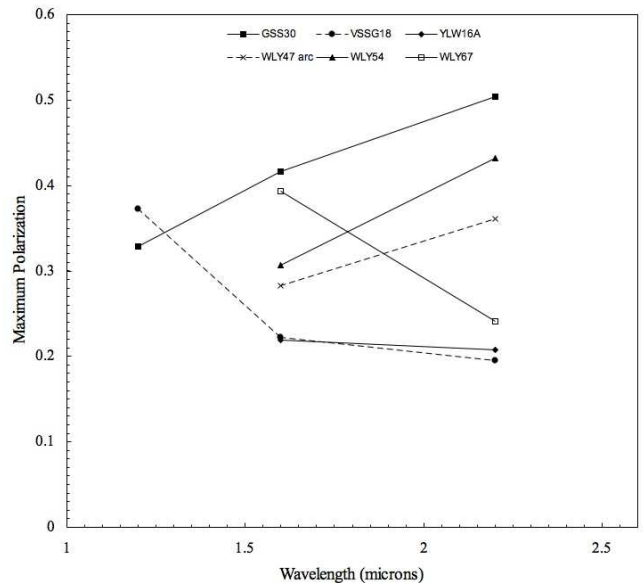


Figure 10. Wavelength dependence of the maximum polarizations, for spatially resolved sources. Class I and Class II YSOs are represented with solid and dashed lines, respectively. The behaviour of the maximum polarization suggests that in the outer regions of the YSOs scattering is important.

a rising or flat polarization with increasing wavelength is predicted by the Mie theory for single scattering by sub-micron grains with a range of sizes. In VSSG18 there is a decrease in the polarization between 1.2 μm and 2.2 μm , between 2.2 μm and 3.8 μm the degree of polarization increases. The same behaviour is observed for WLY54. Three of the objects show no significant change in polarization with wavelength. The first is the Class III object YLW13A, the second is the Class II object DOAR25, and the third is the Class II object WLY47. The polarization levels for both YLW13A and DOAR25 are very low, $P \sim 1\%$, whereas the degree of polarization determined for WLY47 is $P \sim 5\%$. The Class I object YLW16A shows only a one percent change in polarization between 1.6 μm and 2.2 μm , $P_H \sim 11\%$ and $P_K \sim 10\%$. However, the level of polarization is shown to significantly decrease between 2.2 μm and 3.8 μm , $P_{LP} \sim 3\%$. The same trend is seen for the Class I object GSS30 between 1.2 μm and 1.6 μm ; only a one percent change in polarization is observed, with larger decreases seen after 1.6 μm .

Figure 10 shows the wavelength dependence for the maximum polarizations for the 6 objects with extended nebulae. The degree of polarization is seen to increase with increasing wavelength for three of the sources. One of the YSOs shows little change in polarization with wavelength; the remaining two objects display a decrease in polarization with wavelength. Of the three sources showing a positive slope two are Class I and extended, the third is the extended arc of nebulosity that is located close to the Class II object WLY47. WLY47 is typically given a Class II designation, however the spectral index $\alpha = 0.17$ puts WLY47 in the transition object regime and the aperture is across the arc of nebulosity. The first object that shows a definite negative slope is the Class II object VSSG18. The other object that has a negative slope is WLY67; it should be noted that the

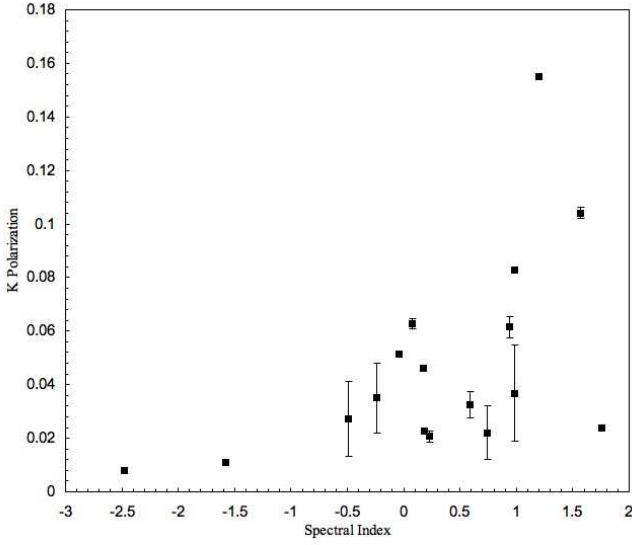


Figure 11. A comparison of the degree of core polarization in the K waveband for each object with its spectral index assessed in the wavelength range $2\ \mu\text{m}$ to $14\ \mu\text{m}$. Error bars are shown for the degree of K polarization; where no error bar is visible the error is too small to be seen outside the point. The higher the degree of core polarization the more positive the spectral index.

polarization data in the K band is poor quality. YLW16A shows only a 1% decrease in polarization. This could be explained as a result of the proximity of the aperture centre to the polarization disc; the data for YLW16A only cover the inner region of the envelope.

Figures 9 and 10 suggest that in the inner regions of YSOs dichroism is an important mechanism in the production of polarized light. However, we caution that this conclusion might be false if there are spatially unresolved scattered light structures with complicated polarization patterns. In the outer envelopes scattering is usually dominant. With the exception of the arc of nebulosity close to WLY47 all the sources that display core polarization levels above $P_{core} \sim 4\%$ have negative slopes between $1.2\ \mu\text{m}$ and $2.2\ \mu\text{m}$. The sources that display negative slopes to their maximum polarizations have $P_{max} < 30\%$; aside from VSSG18 the apertures for determining the maximum polarization are centred no more than 4 arcseconds from the flux peak.

4.9.2 Evolutionary Indicator

The current method used to determine the evolutionary stage of an YSO is based on a combination of the shape of its IR SED and its spectral index; both are dependent on the distribution of circumstellar material. Generally, the degree of core polarization is seen to decrease as the age of the YSO, as indicated by the IR classification, increases. The Class I sources typically display polarizations in the range $1\% < P_K < 20\%$, Class II sources $1\% < P_K < 6\%$, and the only Class III source has $P_K < 1\%$. The wavelength dependence for the core polarizations in the unresolved sources has shown that the polarization very probably has a strong dichroic component. The lower polarizations and unresolved structure in the Class II sources probably indicate an evolutionary change to dichroic extinction as the dominant source

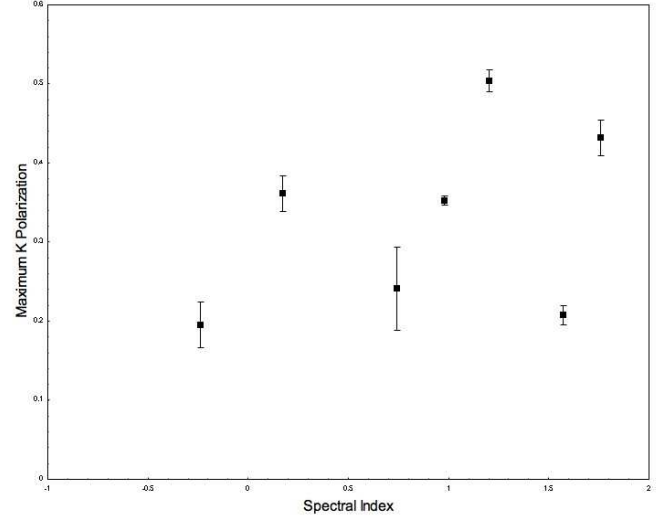


Figure 12. A plot of the maximum degree of polarization in the K waveband for each object with extended nebulosity against the spectral index assessed in the wavelength range $2\ \mu\text{m}$ to $14\ \mu\text{m}$.

of polarization, contrasting with scattering in the Class I sources. The main difference in the dust properties of the Class I and Class II stages of evolution is thought to be only that the circumstellar envelope has dissipated, leaving only the disc.

Again we caution that that Class designations are empirical and are influenced by the system inclination as well as the evolutionary status. Physically, the spectral index depends as much on the optical depth in the line of sight to the protostar as the actual structure of the circumstellar matter. Systems viewed in the equatorial plane (i.e. with an edge-on disc) will display a more steeply rising SED, higher polarization and higher optical depth, than pole-on systems, which may lead to mis-classification.

Figure 11 compares the degree of polarization in the K band for all the sources against their spectral indices, α_{2-14} . As discussed in §1.2.1, the spectral index is the slope of the infrared spectral energy distribution (IR SED) and is commonly assessed in the wavelength range $2\ \mu\text{m}$ to $10\text{-}25\ \mu\text{m}$. The subscript (2-14) indicates that the spectral indices plotted are assessed in the wavelength range $2\ \mu\text{m}$ to $14\ \mu\text{m}$, where the longer wavelength is based on the ISO $14\ \mu\text{m}$ filter. The degree of polarization tends to increase with increasing α_{2-14} ; this trend is also observed in the H and Lp wavebands and is suggested by the limited J band data available. It is important to note that the majority of the sources in the sample have $\alpha_{2-14} > 0$, only four of the sources observed have $\alpha_{2-14} < 0$.

The maximum degree of polarizations observed for each YSO in the K band is compared to their α_{2-14} in figure 12. The maximum polarization of an YSO with extended nebulosity does not appear to be dependent on its IR evolutionary stage. The same is also seen with the H band polarization. α_{2-14} maps the warm gas component, whereas the extended nebulosity represents the cold gas component.

Figures 11 and 12 show that the degree of polarization cannot be used to independently determine the evolutionary stage of an object, but it can be used to provide an approx-

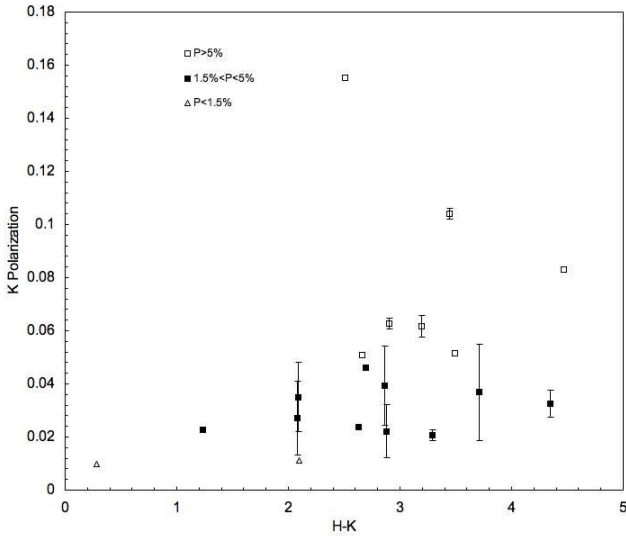


Figure 13. A comparison of the degree of core polarization of each object in the K waveband with its H-K colour. The open triangles indicate sources with $P_K < 1.5\%$, filled squares indicate sources with $1.5\% > P_K > 5\%$, and open squares indicate sources with $P_K > 5\%$. Error bars are shown for the degree of K polarization; where no error bar is visible the error is too small to be seen outside the point. The lowest core polarizations are observed for the sources with lower H-K colours, and the highest core polarizations are observed for the sources with the largest H-K colours.

imate guide. The older objects typically display lower core and maximum polarizations. Polarizations of $P > 6\%$ are only seen for Class I YSOs.

4.9.3 Polarization as a Function of Colour

One of the advantages of conducting the survey in the ρ Oph region is that complete near-IR J, H, K, and L spectral information is available for each source (see Wilking, Lada & Young 1989; Greene et al. 1994; Barsony et al. 1997). This enables comparisons between the polarimetric and spectral data. In figure 13 the degree of polarization in the K band for each source is compared with its H-K colour. The H-K colour is a measure of the redness of the source. The redness of an YSO decreases as it evolves. Therefore, the H-K colour is an indicator of the age of an YSO. There is a positive trend observed between the polarization and H-K colour. The sources that display the highest levels of polarization have $H-K > 2.5$, the sources that have polarizations between 1.5% and 5% have the greatest range of H-K colours. Of the two sources that show polarizations of less than 1.5% one has $H-K = 2.1$, and the other has the lowest H-K colour of any of the sample ($H-K \approx 0.3$).

In figure 14 the near-IR colour-colour diagrams for the ρ Oph sample sources are presented with K band polarization measurements. The open triangles indicate sources with polarization less than 1.5%, filled squares represent sources with polarization between 1.5% and 5%, and open squares indicate sources with polarization greater than 5%. The colour-colour plots indicate that the polarization correlates with near-IR excess emission, as measured by the H-K

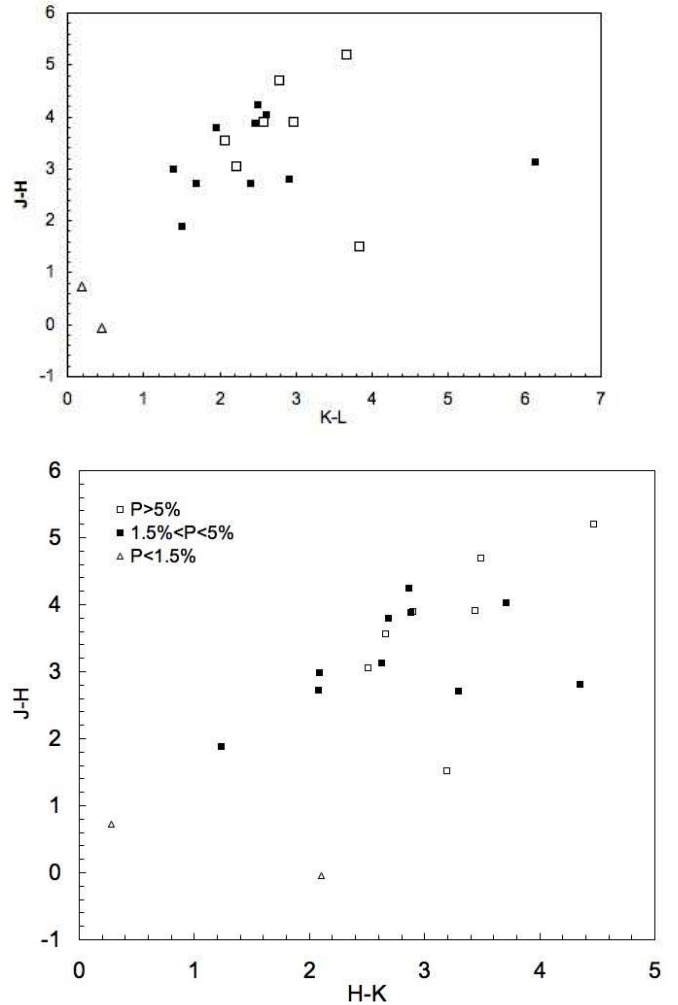


Figure 14. Near-IR colour-colour diagrams with K core polarization measurements. The open triangles indicate sources with $P_K < 1.5\%$, filled squares indicate sources with $1.5\% > P_K > 5\%$, and open squares indicate sources with $P_K > 5\%$.

and K-L colour index. All sources with $K-L \geq 1.5$ have $P_K \geq 1.5\%$. Aside from DOAR25 all stars with $H-K \geq 1.2$ also have $P_K \geq 1.5\%$.

5 MODELS

The shadow.f code (Lucas et al. 2004; Lucas 2003) can be used to represent a YSO with either 2-D, axisymmetric model or a 3-D, non-axisymmetric model. The distribution of matter is based on a simple star, disc, envelope system. The grains in the system are oblate spheroids; their appearance does not change with rotation about the short axis. It is assumed that the short axis of the grains is perfectly aligned with the magnetic field and that the grains spin about this axis. Large numbers of photon packets are generated at the surface of the protostar and these then move through the system, suffering modifications to their Stokes vectors due to dichroic extinction and scattering events.

The model results produced by the shadow.f code are output as Stokes I, Q and U images for comparison with the

observational data. The pixel scale applied to the Stokes parameters is the same as that for the UKIRT polarization data; 0.286 arcseconds pixel⁻¹ or 0.143 arcseconds pixel⁻¹ with the magnifier in place (the distance to ρ Oph is assumed to be 160 parsecs). The Stokes I, Q, U are convolved using a Moffat profile with the form

$$\frac{1}{\left(1 + \left(\frac{R}{\alpha}\right)^2\right)^\beta} \quad (3)$$

where α and β are two constants determined from the point-spread-function (PSF) of a standard star. The POLPACK package is then used to produce the degree of polarization map and the vector catalogue.

5.1 Input Parameters

The shadow.f code uses numerous input variables, which are listed in Table 4. The recommended minimum number of input photons is 100,000. The radius of the system (i.e. the large scale envelope), the outer radius of the disc, the base radius and the opening angle of the cavity manipulate the physical dimensions of the system. All four variables can be estimated from the observational results. The polar and azimuthal viewing angles can also be estimated from the data. A polar viewing angle of 0 or 180 degrees means that the observer is looking towards the pole of the object, an angle of 90 degrees provides an edge on view of the system. The density coefficient and the vertical density gradient are used to manipulate the structure of the envelope and its optical depth.

5.2 Density Distribution

The code has been adapted so that it can use two different envelope density equations. The first is an empirical distribution that uses a power law index to fix the vertical density gradient.

$$\rho_{env} = CR^{-3/2} \left(\frac{1}{\mu^k + 0.05} \right) \quad (4)$$

where C is a free parameter whose value is the density coefficient in units of kg m^{-3/2}. In most cases the line of sight to the protostar passes through the envelope but not the accretion disc, so C is simply proportional to τ_K , the optical depth at K band, which is one of the parameters listed in Table 4. R is the 3-dimensional radius for the natural system of cylindrical polar coordinates defined by the disk rotation axis ($R = \sqrt{r^2 + z^2}$); the azimuthal coordinate is Λ , $\mu = z/r$, and k is the power law index (increasing the value of k increases the degree of flattening of the envelope).

The second is based on the density distribution of Terebey, Shu and Cassen (1984),

$$\rho_{env} = CR^{-3/2} \left(1 + \frac{\mu}{\mu_0} \right)^{1/2} \left(\frac{\mu}{\mu_0} + \frac{2r_c\mu_0^2}{R} \right)^{-1} \quad (5)$$

where r_c and μ_0 are as described in that paper. Models that employ Equation 5 do not use the power law index, k , that is listed in Table 4 but replace this parameter with the ‘‘centrifugal radius’’ r_c .

5.3 YLW16A

The bipolar nature of this system can be inferred from the polarization maps and polarized flux maps in figure 4(b-c). However, the image in figure 4(a) does not resolve the structure, so we illustrate it better with additional data shown in figure 15(a-b). Figure 15(a) shows a NICMOS image at 0.15 arcsec resolution from the HST archive. The central regions of the system are seen to be double peaked. Figure 15(b) shows a deep ground based image of a wider area reproduced from Lucas & Roche (1998), with slightly higher spatial resolution than the polarimetric data in figure 4. This image shows the arrowhead structure mentioned in §4.4.

5.3.1 Model Parameters

Models with an evacuated cavity along the system axis (the default assumption) failed to qualitatively reproduce either the arrowhead structure or the double-peaked nature of the core. We therefore attempted to reproduce these features by modelling YLW16A as a bipolar source with a dusty jet inside the bipolar cavity. Dust was introduced into both lobes of the bipolar cavity. Low density dust in the western lobe of the cavity (the part tilted away from the line of sight) reflects light from the protostar that would otherwise escape the system unseen, and serves to increase the prominence of the western peak. High density dust in the eastern lobe is used to increase the obscuration of the protostar and the eastern part of the reflection nebula so that the jet feature produced by dust in the western lobe appears relatively bright. The eastern lobe is slightly curved in the parabolic sense with cavity walls at:

$$r = R_c + |z| \tan(\theta_c) \left(\frac{R_c}{R} \right)^{cc} \quad (6)$$

where θ_c is a parameter equivalent to the opening angle close to the disc plane, R_c is the radius of the cavity in the disc plane, and cc is the parabolic curvature parameter. The dust in the eastern lobe is located throughout the cavity from the stellar surface to a radius, $R=1000$ AU, but only for azimuthal angles $|\Lambda| < 100^\circ$ ($\Lambda=0$ is the azimuth of the line of sight). This increases the extinction toward the inner regions of the eastern lobe, while allowing some light through to illuminate the large scale reflection nebulosity that is observed. In order to better reproduce the narrow jet-like feature seen in figure 15) in the western lobe, the cavity on that side has a narrow cylindrical structure described by $r < R_c$ and dust fills the region at:

$$R_{CD} < R < 270 \text{ AU}. \quad (7)$$

with density $\rho_{cav} = 3 \times 10^{-13} G_{CD}$. The density in the eastern lobe of the cavity is:

$$\rho_{cav} = 3 \times 10^{-13} G_{CD2} \left(1 + \left(\frac{R}{R_c} \right)^2 \right)^{-1} \text{ kgm}^{-3} \quad (8)$$

where G_{CD} and G_{CD2} are free parameters, with CD referring to cavity dust.

The Moffat profile used to convolve the Stokes elements

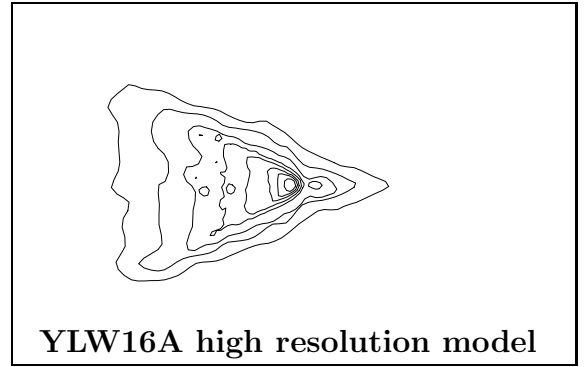
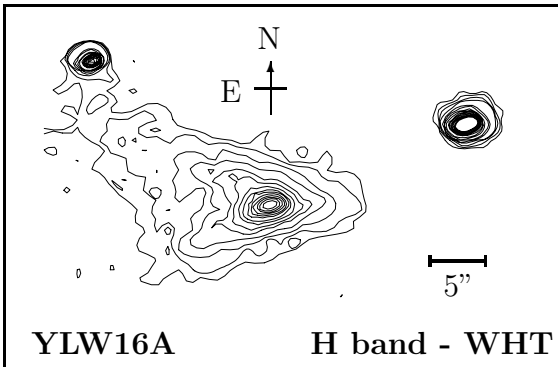
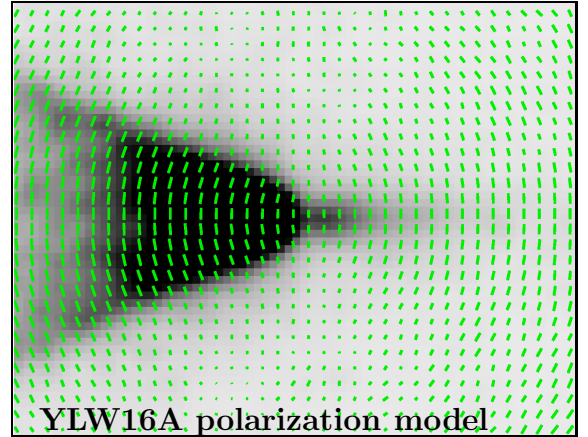
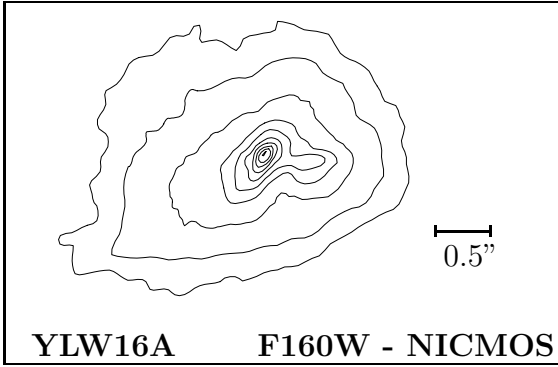


Figure 15. Images of YLW16A. (top) NICMOS image in the F160W filter, showing the bipolar nature of the system. We interpret the small scale narrow extension in the western lobe as reflection from a dusty jet. Data from the HST archive (programme xxxx, PI S.Terebey). (bottom) Wider field H band image reproduced from Lucas & Roche 1998. This image shows the extended nebulosity and the arrowhead structure more clearly than the polarimetric data in figure 4. The figures have the same orientation as the data in figures 1 and 4, i.e. north is up and east is to the left.

was described by $\alpha = 6.49$ and $\beta = 3.35$. These values were determined from the point spread function (PSF) for the point-like young star YLW16B imaged on the same night as YLW16A.

5.3.2 Model Fit

The final model provides a quantitative fit to the position angle of the polarization vectors and degree of polarization over the core, which was assessed in a 2 arcsecond aperture and is centred at the point between the two peaks. In addition it provides a quantitative fit to the maximum polarization assessed in a 0.5 arcsecond aperture centred approximately 3.5 arcseconds from the core.

The model fit to YLW16A is shown in figure 16, the fit parameters are summarised in table 4.

The model provides a qualitative fit to the total flux distribution and the polarized intensity distribution. By placing

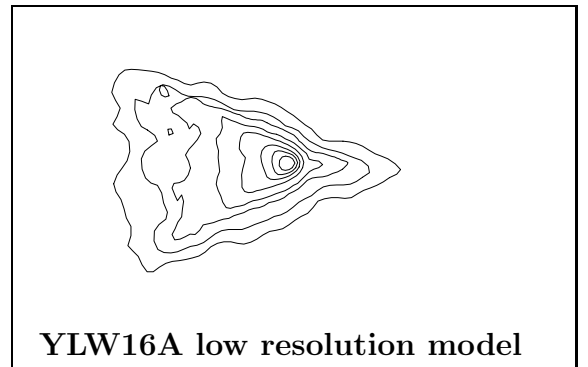


Figure 16. The model fit for YLW16A. (top) polarization vector map, smoothed to the approximate resolution of the data in figure 4. The toroidal field structure reproduces the prominent polarization disc. (middle) flux distribution, shown at the approximate resolution of the NICMOS image. Note that we do not attempt to reproduce the northwest-southeast orientation of the inner contours seen in figure 15. (bottom) flux distribution shown at the approximate resolution of the ground based data. The figure has the same orientation as figure 15.

Table 4. Parameters for model fit to YLW16A at the K band.

Parameter	Value
System Radius	3400 AU
Outer Radius of Disc, r_o	100 AU
Envelope Optical Depth to protostar at K, τ_K	8.6
Power Law Index, k	0
Polar Viewing Angle, θ	$66^\circ.4$
Azimuthal Viewing Angle, Λ	0°
Base Radius of Cavity, R_c	25 AU
Half-opening Angle of Cavity at base, θ_c	25°
Grain Albedo	0.4
Grain Axis Ratio	$1.015 > gr > 1.03$
Maximum Grain Size	$1.05 \mu\text{m}$
Minimum Radius of Cavity Dust, R_{CD}	25 AU
Lower cavity Density Coefficient, G_{CD}	0.1
Upper cavity Density Coefficient, G_{CD2}	6
Parabolic Curvature Parameter, cc	0.2

dust in both cavities it was possible to reproduce the second peak seen in the NICMOS data. If dust was placed in only the western (right hand) lobe it was not possible to reproduce the second peak for any value of G_{CD} investigated, hence the need for the dense dust in the eastern lobe. The fit is achieved for values of the upper and lower density coefficients of $G_{CD2} = 6 \pm 1.5$ and $0.01 < G_{CD} < 0.1$. We note that the second peak is less prominent in the model than in the NICMOS data, so we do not rule out the possibility of a second illuminating source at that location.

The best fit parameters are listed in Table 4. By comparing the prominence of the eastern and western lobes as seen in the ground based data in figure 4 and figure 15, the polar viewing angle was constrained to $60^\circ \leq \theta \leq 73^\circ$. In the final model a polar viewing angle of $\theta = 66^\circ$ ($\cos(\theta)=0.4$) was found to provide the best fit to the data. The opening angle of the cavity for the final model was $\theta_c = 25^\circ$ (from the disc axis to the cavity wall), and the value of R_c was 25 AU.

The Terebey, Shu & Cassen envelope density equation (5) and the empirical envelope density equation (4) were both investigated. Both equations were capable of producing similar results. The final model used the empirical equation with a power law index of $k = 0$. More positive values of the power law index failed to reproduce the double peaked structure. The Terebey, Shu & Cassen density equation was capable of providing a qualitative fit to the arrowhead structure for a centrifugal radius of $R_c \leq 100$ AU, which approximates to the simple $R^{-3/2}$ distribution as the final model as $R_c \rightarrow 0$.

The total optical depth to the protostar, including the contributions of the cavity dust and the envelope, is $\tau_K = 18$, so the protostar itself is entirely obscured from our line of sight. The optical depth must be lower along other lines of sight to permit the illumination of the large reflection nebula, which is why the cavity dust in the eastern lobe is restricted to a certain range of azimuthal angles, as noted earlier.

The optical depth through the envelope to the protostar in the K band was investigated for values of the envelope density coefficient C that correspond to optical depth $4.6 \leq \tau_K \leq 10.3$ in the models (neglecting the optical depth of the dust inside the cavity). For the preferred range of polar

viewing angles it is possible to reproduce the double peaked structure for an envelope optical depth of $\tau_K = 8.5 \pm 0.4$. The reproduction of the arrowhead structure, without reproducing the double-peaked structure, increases the range of acceptable optical depths to $8.0 \leq \tau_k \leq 9.5$. Decreasing the optical depth of the envelope below this range resulted in a total flux distribution that was dominated by the flux from the western peak and a broadening of the lower lobe, thus the arrowhead shape disappeared. Increasing τ_K above this range resulted in a less prominent western peak and no distinct arrowhead structure.

In the final model the dust grains were aligned with a toroidal magnetic field. An axial magnetic field was able to reproduce the polarization vector structure in the extended nebula, but failed to reproduce the core polarization structure. The outer and inner polarization vector structure is quite successfully reproduced by either a toroidal field or simply a uniform interstellar field oriented parallel to the disc plane. The actual field structure may well be more complicated than this: as noted in §4.4 the the inner contours of the flux distribution have a northwest-southeast orientation (see figure 4a and figure 15, top panel) which is inclined with respect to the larger scale east-west structure. This northwest-southeast orientation of the inner regions is also in the polarization vectors. Our description of the field structure as toroidal is only approximate, given that the orientation of the disc plane is clearly somewhat uncertain. We note that while field lines approximately parallel to the disc plane appear to be required on scales of a few hundred AU, the field structure may of course become more axial on larger scales. The possible existence of a second protostar at the location of the second peak in the NICMOS data is not expected to significantly influence the polarization maps, since the 0.5 arcsec from the principal flux peak is unresolved in the ground based data.

The observed polarization pattern and polarization levels associated with YLW 16A can be well-modelled using dust grains with a maximum size of $1.05 \mu\text{m}$. Smaller maximum grain sizes were considered, however they resulted in core polarizations that were higher than required. The grain axial ratio adopted was $1.015^{+0.015}_{-0.005}$. Grain axial ratios above or below this range led to core polarizations that were significantly higher or lower than required, respectively. Note that since these grains are almost spherical, the magnetic field direction only affects the core polarization and has negligible effect on the other model parameters. It is of course possible that the core polarization is due to grains which are highly aspherical but only weakly aligned with the magnetic field.

5.4 WLY54

5.4.1 Model Parameters

In Figure 5 there is an oblique angle between the normal to the polarization disc plane and the extended nebula. We suggest that this could be explained if WLY54 is a bipolar nebula with a foreground extinction cloud. The vectors reveal the possible existence of a small counterlobe to the southwest of the core. The position angle of the polarization disc relative to the direction of the extended nebula would be explained if there were a source of extinction to the north

of WLY54 that obscures part of the nebula. Further support for the bipolar nature of WLY54 comes from the east - west orientation of the degree of polarization map, which shows a low polarization region running north - south, with two higher polarization regions to either side. The bipolar nature of WLY54 is further supported by the appearance of the less prominent (western) lobe in an H-K colour map (not shown) which appears to be redder than the more prominent (eastern) lobe. However, there is no direct evidence for the foreground extinction cloud that is used in the model to reproduce the unusual total flux and polarization structures. If there is no foreground extinction cloud then something else must be responsible for the misalignment between the disc axis and the extended nebulosity. Two possible explanations are that the orientation of the extended nebulosity is influenced by source movement through a dense medium, or extinction within the cavity. Alternatively, the polarization disc may not be a feature of the system at all, but might simply be due to foreground dichroic extinction if the polarization intrinsic to the WLY54 system is very low in that region. We note that most of the sources in this ρ Ophiuchi sample have redder colours than the sources in the Taurus sample of Whitney et al.(1997), which implies higher foreground extinction. This is particularly obvious for the Class II systems, which have less intrinsic extinction.

The location of the foreground extinction cloud along the line of sight is defined by somewhat arbitrary limits in the model (see Table 5). The structure of the extinction cloud in the plane of the sky is described by a gradient that begins 200AU to the north of the core. Two extinction gradients were investigated. The first is an exponential profile described by

$$\rho_{screen} = C\tau_s e^{\Lambda} \quad (9)$$

where C is a constant (here given the value 4.55×10^{-15} kg m $^{-3}$), τ_s is a variable that can be used to manipulate the optical depth of the extinction cloud, and Λ describes the azimuthal angle. The second is a linear profile

$$\rho_{screen} = C\tau_s r \sin\Lambda \quad (10)$$

where the constant C is here given the value 3×10^{-29} kg m $^{-4}$, and $r \sin(\Lambda)$ is the distance north of the protostar.

It was assumed that the density distribution of the envelope is adequately described by the empirical density equation (10).

The Moffat profile values are determined from the PSF for the point-like YSO YLW13A imaged during the same observing run as WLY54 ($\alpha = 3.71$ and $\beta = 3.49$).

5.4.2 Final Model

The parameters that provide the fit to the H band data are summarized in Table 5 and the fit is illustrated in figure 17.

The model provides a quantitative fit to the maximum degree of polarization in WLY54 (evaluated in a 0.5 arcsecond aperture), and the position angle and degree of polarization of the polarization disc (evaluated in a 2 arcsecond aperture).

The model provides a qualitative fit to the shape of

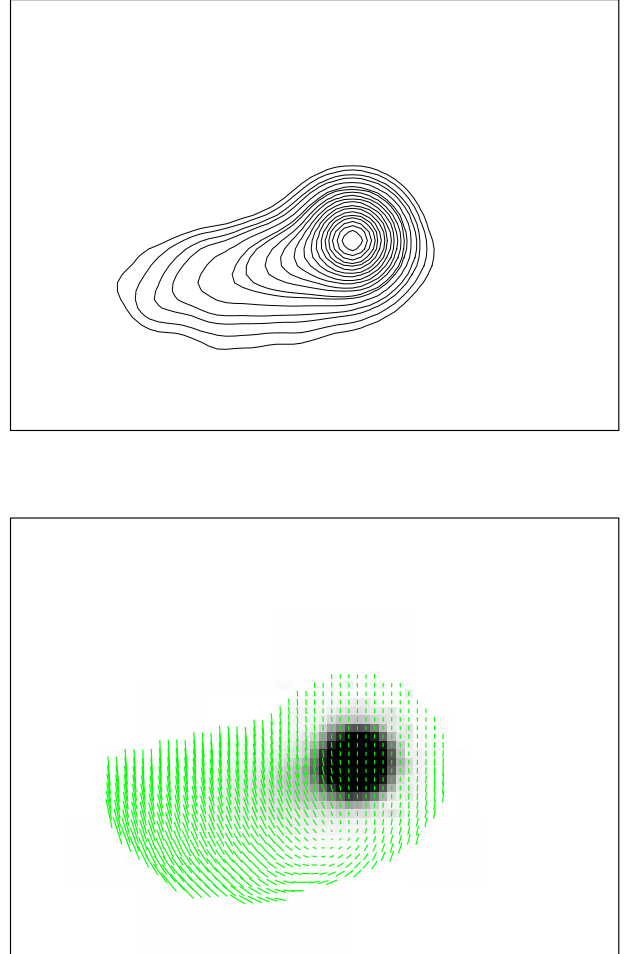


Figure 17. The model fit for WLY54 (top) flux distribution, and (bottom) polarization vector map.

the cometary nebula as revealed by the total flux distribution. In addition the model successfully reproduced the angle between the orientation of the polarization disc and the direction of extension. These features are reproduced by introducing a foreground extinction cloud to the north of the system. The structure of the total flux distribution was best reproduced when the influence of the foreground extinction cloud was described by the linear profile defined in equ.10. The exponential profile did not have a significant influence on the structure of the total flux of WLY54. It was also found that parabolic cavity walls produced a better fit than conical cavity walls. The parabolic cavity walls are defined by equ.6, which introduces a curvature parameter cc to the conical profile.

The cometary appearance of WLY54 suggested a polar viewing angle that minimises the amount of counterlobe that was visible. The possible presence of the foreground extinction cloud in the system means that the polar viewing angle is not tightly constrained since acceptable results were found for $\theta = 45^{\circ}.6_{-9}^{+14}$. The adopted polar viewing angle for the final model provided the best fit to both the total intensity distribution and the polarization data.

Table 5. Parameters for model fit to WLY54 at the H band.

Parameter	Value
System Radius	1560 AU
Outer Radius of Disc, r_o	100 AU
Optical Depth to protostar at H, τ_H	5.95 ± 0.55
Power Law Index	1.0 ± 0.4
Polar Viewing Angle, θ	$45^\circ.6$
Azimuthal Viewing Angle, Λ	0°
Base Radius of Cavity, R_c	30 AU
Half-opening Angle of Cavity at base, θ_c	23°
Parabolic Curvature Parameter, cc	0.2
Grain Albedo	0.45
Grain Axis Ratio	1.015
Maximum Grain Size	$0.35 \mu\text{m}$
Inner Radius of Extinction Cloud	2180 AU
Outer Radius of Extinction Cloud	4680 AU
Density parameter of Extinction Cloud, τ_s	30

A suitable qualitative fit to the total flux distribution was found for a power law index of $k = 1.0 \pm 0.4$ (see Equ.4). Increasing k reduces the prominence of the western lobe for the chosen optical depth.

To produce a reasonable fit to the radial intensity profile of the H band data requires an optical depth in the range $5.4 < \tau_H < 6.5$. Optical depths outside this range either resulted in a total flux distribution that had too steep an intensity profile, for $\tau_H < 5.4$, or too shallow an intensity profile, for $\tau_H > 6.5$. The main problem encountered when trying to further constrain the optical depth was the extremely low levels of core polarization shown by WLY54 at all wavelengths. The best fit to the radial intensity profile is achieved for an optical depth closer to $\tau_H = 6.5$, whereas the best fit to the polarization data is achieved for an optical depth of $\tau_H = 5.5$.

The dust grain albedo was treated as a free parameter. The grains were a mixture of silicates and amorphous carbons. For the polar viewing angle adopted, $\theta = 45^\circ.6^{+14}_{-9}$, the best fit to the data was found for a grain albedo of approximately 0.45 at H.

The position angle of the polarization disc and the outer polarization vector structure were reproduced by dust grains aligned with a toroidal magnetic field. An axial magnetic field led to the position angle of the polarization vectors over the core being at 90° to the requirement due to dichroic extinction. We note that a return to an axial field structure is of course possible on larger spatial scales, and is expected from basic star formation theory. To fit the core 5.3% polarization observed at UKIRT in the H band with the adopted magnetic field structure and maximum grain size of $0.35 \mu\text{m}$ required that the grain axial ratio was not larger than 1.015. Increasing the grain axial ratio resulted in core polarization levels that were significantly larger than required. A fit to the degree of core polarization and position angle of the polarization disc was also found using larger grains. However, the models with larger grains were not able to reproduce the high polarization observed over the more extended envelope.

Spherical grain models were capable of producing a reasonable approximation to the WLY54 data. However, there are some key problems. The model fails to reproduce the polarization vector structure over the core region, and the degree of core polarization is approximately one tenth of

the requirement. The model does manage to reproduce the maximum polarization and provides a qualitative fit to the total flux distribution. To fit the 5.3% polarization requires an optical depth of $\tau = 8.7 \pm 0.6$. The polarization vector structure for an optical depth in this range is comparable to the data. However the model does not provide a good fit to the observed flux distribution.

The density parameter of the foreground extinction cloud was investigated across a broad range of values, $5 \leq \tau_s \leq 50$, as it was not known how its presence would affect the system. Increasing the value of τ_s causes a reduction in the flux from both lobes to the north of the core. The final model required that the density parameter was $\tau_s = 30 \pm 3$ to reproduce the structure of the total flux distribution in the eastern lobe. For the range of optical depths that were capable of reproducing the total flux distribution in the eastern lobe the foreground extinction cloud completely suppressed the appearance of the western lobe at all polar viewing angles for $k \geq 1.0$. For $k = 0.6$ and $\theta = 53^\circ.1$ a small western lobe is visible.

Increasing the cavity curvature parameter results in a narrowing of the extended nebulosity, a qualitative fit to the total flux distribution is found for $cc = 0.2$ when combined with the influence of the foreground extinction cloud.

5.5 EL29

5.5.1 Model Parameters

EL29 was modelled as a bipolar source. The density distribution of the envelope was assumed to be adequately described by the empirical density equation, equ. 4. The structure of the cavity was assumed to be conical ($\tan(\theta_c) = ((R - R_c)/|z|)$). The base radius and opening angle of the cavity were estimated from the polarized flux data for EL29.

A system radius of 1035 AU was estimated from the extent of the degree of polarization map, due to the point-like appearance of the total flux distribution. The point-like nature of the flux distribution makes it difficult to determine the inclination angle of the system. For this reason EL29 was investigated as both a pole-on and edge-on object. An object that is near pole-on would have a more point-like structure similar to that seen in the data. However, if EL29 is a source whose true nature is obscured either due to the faintness of the nebulosity or the limited sensitivity of the observing technique then it is also possible that EL29 is closer to edge-on.

The radius of the inner accretion disc, R_a , was investigated for values between 50 and 600 AU, which is the range of possible values suggested by Ceccarelli et al. (2002).

The dust grains are oblate spheroids that are perfectly aligned by a magnetic field. The magnetic field was investigated with both an axial and toroidal structure. The albedo of the grains was treated as a free parameter.

The final Stokes images (I, Q and U) were convolved using a Moffat profile described by $\alpha = 4.08$ and $\beta = 1.86$, for the pole-on models. The values of α and β are determined from the PSF for the point-like UKIRT photometric standard star FS140 (s587-t) imaged during the same observing run as EL29.

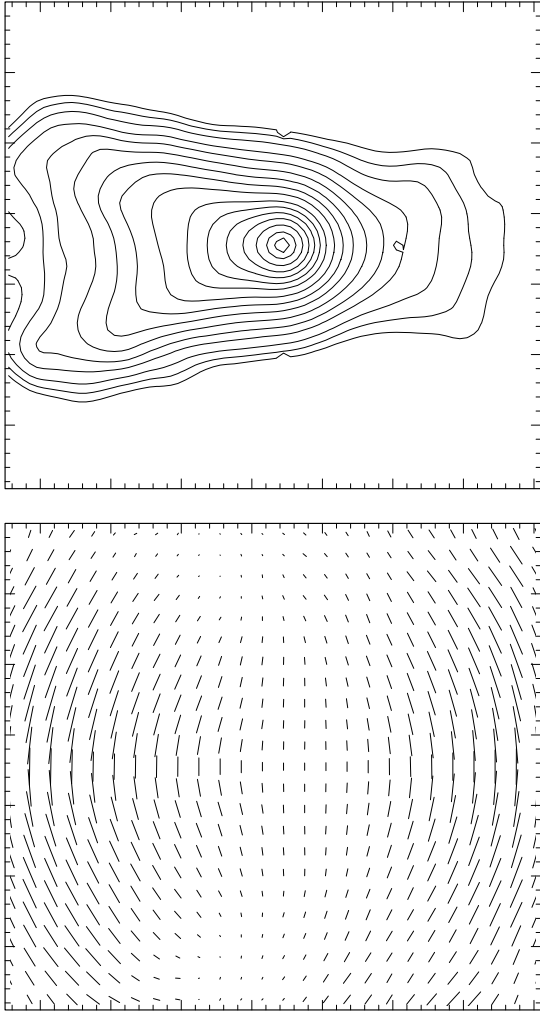


Figure 18. The model fit for EL29 (a) polarized flux distribution, and (b) polarization vector map.

5.5.2 Final Model

The parameters for the final model are given in Table 6. The polarized flux distribution and polarization vector maps for EL29 and the final model are shown in figure 18. The final model provides a quantitative fit to the degree of core polarization, the structure of the polarization vectors and the maximum polarization measured in each lobe. A qualitative fit is provided to the polarized flux distribution. The fit is achieved by modelling EL29 as a system that is neither pole-on nor edge-on and has an outer disc radius of 50 AU.

The inclination of the system was investigated for polar viewing angles in the ranges $0^\circ < \theta < 60^\circ$ (near pole-on) and from $80^\circ < \theta < 90^\circ$ (edge-on). The point-like nature of EL29 in the Stokes I image was not successfully modelled; instead the focus was turned to modelling the polarized flux distribution, the polarization vector structure and the fractional polarization. The inclination angle of the system was determined from previous observations of EL29 that have indicated the presence of a flared disc with $i \leq 60^\circ$ (Boogert

Table 6. Parameters of the model fit to EL29 at the K band.

Parameter	Value
System Radius	1035 AU
Outer Radius of Disc, r_o	50 AU
Optical Depth to protostar at H, τ_K	6.75
Power Law Index, k	0.0
Polar Viewing Angle, θ	$53^\circ.1$
Azimuthal Viewing Angle, Λ	0°
Base Radius of Cavity, R_c	20 AU
Half-opening Angle of Cavity at base, θ_c	20°
Grain Albedo	0.2
Grain Axis Ratio	1.015
Maximum Grain Size	$0.70 \mu\text{m}$

et al. 2002). Acceptable results for the polarized flux distribution and to the maximum polarizations in each lobe were found for an inclination angle of $i = 53^\circ.1_{-8}^{+7}$.

The values of the cavity base radius and half-opening angle investigated were based on the structure of the polarized flux distribution. A reasonable fit to the polarized flux distribution can be found for cavity base radii of and half-opening angles in the ranges $20 \text{ AU} \leq R_c \leq 30 \text{ AU}$ and $20^\circ \leq \theta_c \leq 25^\circ$.

The optical depth to the protostar was investigated between $4 \leq \tau_K \leq 11$. The final model requires that the optical depth is $\tau_K = 7.75_{-1}^{+0.25}$. Optical depths outside this range were not able to reproduce a reasonable fit to the polarized flux distribution.

The empirical density equation was used to determine the density distribution. The power law index was capable of producing acceptable results for $k = 0.0^{+0.4}$. Increasing the power law index (i.e. the vertical density gradient) resulted in a decrease in the prominence of the receding lobe. A more severe flattening of the envelope was not able to reproduce the polarization structure of EL29.

The position angle of the polarization disc was reproduced using dust grains that were aligned with a toroidal magnetic field. Grains aligned with an axial magnetic field were capable of reproducing the vector structure in the outer parts of the polarised flux image but they were not able to reproduce the position angle of the polarization disc. To fit the degree of core polarization, $P_K = 8.3\%$, required that for a maximum grain size of $0.70 \mu\text{m}$ the grain axial ratio be not more than 1.03 for the adopted magnetic field structure. The larger grain axial ratio models and the spherical grain models resulted in core polarizations that were too high or too low, respectively.

The dust grains were a mixture of silicates and amorphous carbons. For the adopted system inclination the dust grain albedo needed to be $\omega_K \leq 0.4$. The final model has an albedo of $\omega_K = 0.2$, which provided the best fit to the polarization data. Increasing the albedo results in an increase in the prominence of the western (receding) lobe.

This model fails to reproduce the point-like flux distribution that we observed for EL29, though we noted in §4.8 that more recent observations have detected the faint extended structure that our model predicts. One possible reason for the faintness of the extended nebulosity is that the adopted envelope structure assumes that there is an axisymmetric distribution of material throughout. However,

the strongly peaked structure of EL29 suggests that there may be a “hole” in the material along the line of sight to the protostar.

6 CONCLUSIONS

The near-infrared linear polarization data for a sample of young stellar objects in the ρ Ophiuchi star-forming region have been analysed. The majority of the objects were spatially unresolved. Five of the objects were clearly associated with extended nebulosity: two of these are bipolar nebulae and three have cometary morphologies.

The extended objects have centrosymmetric vector patterns with a polarization disc over the core. A few of the unresolved objects have polarizations that were too small to detect, with upper limits of 1-2%.

The wavelength dependence of the degree of polarization suggests that dichroism is the dominant mechanism responsible for the polarization of light in the unresolved sources, which constitute the majority of the sample. (The alternative is that these sources have complicated but unresolved polarization structures). In the envelopes of the extended sources the wavelength dependence indicates that scattering dominates the generation of polarized light.

The results of the linear polarimetry survey of ρ Oph were compared to the infrared evolutionary status of the objects. It was found that:

- The distribution of the material around the sample sources does not seem to be strongly correlated with the evolutionary scheme determined by the infrared spectral energy distributions. Point-like structures were seen for objects with Class I, Class II and Class III designations. Five objects were identified as being associated with extended nebulosity. The majority of the extended objects were Class I but one had a Class II designation.

- The near-infrared colour-colour diagrams show that the degree of core polarization is correlated with the H - K and K - L colours.

- A weak correlation is observed between the size of the extended nebulae and the core polarizations.

- There is a positive correlation between the degree of core polarization and the evolutionary stage indicated by the infrared spectral index. Typically, Class I objects show core polarizations in the range $2\% < P_K < 16\%$, whereas core polarizations in the range $1\% < P_K < 6\%$ are seen for the Class II objects, and the only Class III object in the sample shows $P_K < 1\%$. It should be noted that the SED-based assignment of classes is influenced by system inclination as well as evolutionary status.

- A weaker positive correlation between the maximum polarization assessed over the envelopes and the infrared spectral index was also observed.

- Generally, redder sources are associated with higher degrees of core polarization. Those objects that have $P_K \geq 5\%$ have (H - K) colours greater than 2.5. Objects with polarizations in the range $1.5\% > P_K > 5\%$ have the greatest range of (H - K) colours ($1 < (H - K) < 4.4$), and the two objects with $P_K \leq 1.5\%$ have $(H - K) < 2.2$ (the object with the lowest H-K also has the lowest P_K).

Similar correlations have been previously identified for

young stellar objects in the Taurus region (Whitney, Kenyon & Gomez 1997). The results presented in this work for ρ Oph and by previous authors for Taurus reveal that the polarization data appears to support the evolution of circumstellar matter predicted in models of low-mass star formation.

The shadow.f code was used to model three Class I objects in ρ Oph that represented a cross-section of the morphologies observed. The first was the bipolar object YLW16A, the second was the cometary object WLY54, and the third was the point-like object EL29. In each case a fit to the polarization data was found by assuming that the objects could all be modelled as a bipolar system.

The point-like source EL29 displays a bipolar polarization pattern across the image profile. This was assumed to be the result of diffuse bipolar nebulosity that was only detectable in polarized light. The presence of diffuse nebulosity has been confirmed by more recent observations. Our model fails to reproduce the point-like total flux distribution but successfully fits the polarized flux distribution and the polarization vector structure.

The results of the modelling revealed that to reproduce the observed total flux distributions and polarization data there were several properties common to the three systems investigated. These properties are:

- The dust grains that are responsible for the polarization of the light are required to be smaller than the wavelength of observation. The maximum grain size was found to be $1.05 \mu\text{m}$.

- The dust grains are either near-spherical or very weakly aligned. More strongly dichroic grains can only be present if the field structure varies along the line of sight to the protostar in a manner that weakens the measured dichroic extinction effects. Our models assume perfect grain alignment with the magnetic field. We find that grains with an axial ratio of more than 1.03 led to significantly higher polarizations than the data. In addition, grains with axial ratios of 1.1 were found to result in little spatial variation in the polarization across the source for parameters that were capable of producing acceptable fits to the flux distributions investigated.

- Spherical grain models were successful at reproducing the flux distributions and polarization vector patterns, but they could not successfully reproduce the fractional polarizations measured in the cores of the YSOs. Typically, the core polarization provided by a spherical grain model was a tenth of the observed value.

- Given that some dichroic extinction is required to reproduce the core polarizations, a toroidal magnetic field structure is necessary in the central regions of the nebula in order to reproduce the orientation of the polarization disc parallel to the accretion disc.

ACKNOWLEDGMENTS

We wish to thank the staff of UKIRT, which is operated by the Joint Astronomy Centre on behalf of the UK Science and Technology Facilities Council (STFC). STFC has taken over the former astronomy functions of PPARC, the Particle Physics and Astronomy Research Council. This research was supported by a PPARC PhD studentship awarded to AFB.

PWL is supported by the STFC via an Advanced Fellowship at the University of Hertfordshire.

REFERENCES

- Allen L.E., Myers P.C., Francesco J.D., Mathieu R., Chen H., Young E., 2002, *APJ*, **566**, 993
- Andre P., Ward-Thompson D., Barsony M., 1993, *APJ*, **406**, 122
- Andre P., Montmerle T., 1994, *ApJ*, 420, 837
- Aspin C., Casali M.M., Walther D.M., 1989, in Reipurth B., ed., *ESO Conf. Work. Proc. 33, Low Mass Star Formation and Pre-Main Sequence Objects*, p.349, published by European Southern Observatory, Garching, Germany
- Barsony M., Kenyon S.J., Lada E.A., Teuben P.J., 1997, *ApJSS*, 112, 109
- Bontemps S., Andre P., Terebey S., Cabrit S., 1996, *A&A*, **311**, 858
- Bontemps S., Andre P., Kaas A.A., Nordh L., Olofson G., Hultgren M., Abergel A., Blommaert J., Boulanger F., Burgdorf M., Cesarky C.J., Cesarky D., Copet E., Davies J., Falgrone E., Lagache G., Montmerle T., Perault M., Persi P., Prusti T., Puget J.L., Sibille F., 2001, *A&A*, 372, 173
- Boogert A.C.C., Hogerheijde M.R., Ceccarelli C., Tielens A.G.G.M., van Dishoeck E.F., Blake G.A., Latter W.B., Motte F., 2002, *APJ*, **570**, 708
- Ceccarelli C., Boogert A.C.A., Tielens A.G.G.M., Caux E., Hogerheijde M.R., Parise B., 2002, *A&A*, **395**, 863
- Chrysostomou A.A., Clark S.G., Hough J.H., Gledhill T.M., McCall A., Tamura M., 1996, *MNRAS*, 278, 449
- Chrysostomou A.A., Menard F., Gledhill T.M., Clark S., Hough J.H., McCall A., Tamura M., 1997, *MNRAS*, 285, 750
- Dolidze M.V., Arakeylan M.A., 1959, *SvA*, 3, 434
- Duchene G., Bouvier J., Bontemps S., Andre P., Motte F., 2004, *A&A*, **427**, 651
- Elias J.H., 1978, *ApJ*, 224, 453
- Girart J.M., Rodriguez L.F., Curiel S., 2000, *APJL*, **544**, 153
- Grasdalen G.L., Strom K.M., Strom S.E., 1973, *ApJ*, 184, L53
- Greene T.P., Young E.T., 1992, *ApJ*, 395, 516
- Greene T.P., Wilking B.A., Andre P., Young E.T., Lada C.J., 1994, *APJ*, 434, 614
- Huélamo N., Brandner W., Wolf S., 2007, *Rev.Mex.A.A. Conf. Series.*, 29, 149
- Kamazaki T., Saito M., Hirano N., Kawabe R., 2001, *APJ*, **548**, 278
- Lucas P.W., Roche P.F., 1997, *MNRAS*, 286, 895
- Lucas P.W., Roche P.F., 1998, *MNRAS*, 299, 699
- Lucas P.W., 2003, *J. Quantitative Spectroscopy & Radiative Transfer*, 79-80, 921
- Lucas P.W., Fukagawa M., Tamura M., Beckford A.F., Itoh Y., Murakawa K., Suto H., Hayashi S., Oasa Y., Naoi T., Dori Y., Ebizuka N., Kaifu N., 2004, *MNRAS*, 352, 1347
- Lynds B., 1962, *APJS*, 7, 1
- Ressler M.E., Barsony M., 2001, *AJ*, 121, 1098
- Sekimoto Y., Tatematsu K., Umemoto T., Koyama K., Tsuboi Y., Hirano N., Yamamoto S., 1997, *APJL*, **489**, 63
- Tamura M., Sato S., Suzuki H., Kaifu N., Hough J.H., 1990, *ApJ*, 350, 728
- Terebey S., Shu F.H., Cassen P., 1984, *ApJ*, 286, 529
- Vrba F.J., Strom K.M., Strom S.E., Grasdalen G.L., 1975, *APJ*, 197, 77V
- Whitney B.A., Hartman L., 1993, *ApJ*, 402, 605
- Whitney B.A., Kenyon S.J., Gomez M., 1997, *ApJ*, **485**, 703
- Whitney B.A., Wood, K., Bjorkman J.E., Cohen M., 2003, *ApJ*, 598, 1079
- Wilking B.A., Lada C.J., 1983, *APJ*, 274, 698
- Wilking B.A., Lada C.J., Young E.T., 1989, *ApJ*, 340, 823
- Wilking B.A., Bontemps S., Schuler R.E., Greene T.P., Andre P., 2001, *APJ*, **551**, 357W
- Ybarra J.E., Barsony M., Haisch K.E., Jarett T.H., Sahai R., Weinberger A.J., 2006, *ApJ* 647, L159
- Young E.T., Lada C.J., Wilking B.A., 1986, *ApJ*, 304, L45
- Zhang Q., Wootten A., Ho P.T.P., 1997, *ApJ*, 475, 713

This paper has been typeset from a \TeX / \LaTeX file prepared by the author.